ELSEVIER

Contents lists available at ScienceDirect

Remote Sensing of Environment

journal homepage: www.elsevier.com/locate/rse





Assessment of the impact of discontinuity in satellite instruments and retrievals on global PM_{2.5} estimates

Melanie S. Hammer ^{a,*}, Aaron van Donkelaar ^a, Liam Bindle ^a, Andrew M. Sayer ^{b,c}, Jaehwa Lee ^{d,b}, N. Christina Hsu ^b, Robert C. Levy ^b, Virginia Sawyer ^e, Michael J. Garay ^f, Olga V. Kalashnikova ^f, Ralph A. Kahn ^b, Alexei Lyapustin ^b, Randall V. Martin ^a

- a Department of Energy, Environmental, and Chemical Engineering, Washington University in St. Louis, St. Louis, MO, USA
- ^b Earth Sciences Division, NASA Goddard Space Flight Center, Greenbelt, MD, USA
- ^c Goddard Earth Sciences Technology and Research II, University of Maryland Baltimore County, Baltimore, MD, USA
- d Earth System Science Interdisciplinary Center, University of Maryland, College Park, MD, USA
- ^e Science Systems and Applications (SSAI), Lanham, MD 20706, USA
- f Jet Propulsion Laboratory, California Institute of Technology, Pasadena, CA, USA

ARTICLEINFO

Edited by Dr. Menghua Wang

Keywords:
Remote sensing
Aerosols
Fine particulate matter
MODIS
VIIRS
MISR
MAIAC
Air pollution

ABSTRACT

Exposure to fine particulate matter ($PM_{2.5}$) is the leading environmental risk factor for mortality globally. Satellite-derived estimates of surface $PM_{2.5}$ developed from a combination of satellites, simulations, and ground monitor data are relied upon for health impact studies. The ability to develop satellite-derived $PM_{2.5}$ estimates requires the continued availability of aerosol optical depth (AOD) sources. This work examines the impact of the addition or loss of satellite AOD data sources on global $PM_{2.5}$ estimation and the impact of continuing the long-term record with AOD from the Visible Infrared Imaging Radiometer Suite (VIIRS) on the Suomi-National Polar orbiting Partnership (S-NPP) satellite after the loss of the MODIS (MODerate resolution Imaging Spectroradiometer) and MISR (Multi-angle Imaging Spectroradiometer) instruments on board the Terra and Aqua satellites. We find that the addition of VIIRS S-NPP AOD products to geophysical $PM_{2.5}$ estimates from satellites and simulations causes regional differences that correspond to differences in the VIIRS and MODIS Deep Blue AOD algorithms and sampling. Changes in long-term trends and timeseries due to the addition or loss of AOD data sources are generally within their uncertainties. Statistical fusion with ground monitor data partially corrects for changes due to sampling differences when introducing the VIIRS AOD products, but uncertainty remains over desert regions where ground monitor coverage is sparse. This work provides promise for the sustained development of global satellite-derived $PM_{2.5}$ estimates, despite discontinuities in instruments and retrieval methods.

1. Introduction

Exposure to fine particulate matter ($PM_{2.5}$) is the leading environmental risk factor for the global burden of disease, with an estimated 4 million attributable deaths worldwide in 2019 (Murray et al., 2020). Despite this importance for global health outcomes, ground monitoring of surface $PM_{2.5}$ concentrations remains sparse over much of the world, with very few countries having >3 monitors per million inhabitants and many countries having no regular monitoring at all (Martin et al., 2019). Estimates of surface $PM_{2.5}$ developed from a combination of satellites, simulations, and ground monitor data using a geophysical-hybrid approach have provided the critical high quality and spatially

continuous long-term exposures necessary for health impact studies on both regional (van Donkelaar et al., 2019) and global (van Donkelaar et al., 2021; Hammer et al., 2020; van Donkelaar et al., 2016) scales. These geophysical-hybrid estimates have been relied upon for global health assessments (Murray et al., 2020) and numerous epidemiological studies (Anenberg et al., 2018; Bai et al., 2019; Burnett et al., 2018; Odo et al., 2022; Pappin et al., 2019; Southerland et al., 2022). The ability to consistently extend these geophysical-hybrid PM_{2.5} estimates into the future relies on the continued availability of the data products used as inputs, and in particular the continued availability of reliable, accurate, and consistent long-term satellite-retrieved aerosol information.

Several satellite instruments and algorithms provided long-term

E-mail address: melanie.hammer@wustl.edu (M.S. Hammer).

^{*} Corresponding author.

global aerosol optical depth (AOD) retrievals over recent decades that have been used in the development of geophysical-hybrid PM2.5 estimates. The SeaWiFS (Sea-viewing Wide Field-of-View Sensor) instrument flew on the SeaStar satellite and offered high quality measurements over its lifetime from 1997 to 2010 (Sayer et al., 2012). Twin MODIS (MODerate resolution Imaging Spectroradiometer) instruments on the Earth Observing System (EOS) satellites Terra and Agua have provided AOD retrievals from several algorithms since 2000 and 2002 respectively, while the MISR (Multi-angle Imaging Spectroradiometer) instrument also on board Terra has provided retrievals since 2000. The Terra and Aqua satellites were designed to only have lifetimes of 5 years and 6 years respectively, and both are now drifting from their normal orbits and are scheduled to be fully shutdown by 2025 or 2026 (Sawyer et al., 2020). The continuation of the EOS-era satellite AOD record, and hence geophysical-hybrid PM2.5 estimates, depends on having a suitable replacement.

In late 2011, the Suomi National Polar-orbiting Partnership (S-NPP) satellite was launched carrying the Visible Infrared Imaging Radiometer Suite (VIIRS) instrument. The NOAA20 platform, carrying another VIIRS instrument, was launched in late 2017 and more are planned to launch and fly over the decades to come. VIIRS was designed to have similar capabilities to MODIS. However, there are issues which cause differences between retrievals from the two instruments:

- 1) Calibration: Even two identical instruments will have differences in calibration and changes in performance over time; for example, this has historically caused offsets and differential trending in retrievals from the two MODIS sensors (e.g. Lyapustin et al., 2014; Sawyer et al., 2020; Sayer et al., 2019). At present, there is a considerable calibration difference among MODIS Aqua, SNPP VIIRS, and NOAA-20 VIIRS sensors (e.g Xiong et al., 2020).
- 2) Retrieval processes: There are a few key differences that complicate obtaining a consistent retrieval between VIIRS and MODIS, including differences in spectral bands and field-of-view (Hsu et al., 2019; Sawyer et al., 2020; Sayer et al., 2019). Differences in individual retrieval algorithms will also contribute. For example, the VIIRS Deep Blue V1 algorithm includes updates to the aerosol and surface models used in the retrieval that did not make it into the release of MODIS C6.1 Deep Blue (Sayer et al., 2019), as NASA's reprocessing schedules for the missions are not synchronized. The differences in spectral bands between VIIRS and MODIS results in a difference in the cloud mask used in VIIRS Dark Target vs MODIS C6.1 Dark Target (Sawyer et al., 2020).
- Sampling: VIIRS has a larger swath width than MODIS, resulting in no data gaps at equatorial regions and twice or more sampling per day at middle to high latitudes (Hsu et al., 2019).

Despite these challenges the MODIS Dark Target and Deep Blue AOD retrieval algorithms have been successfully ported to process VIIRS S-NPP measurements (Hsu et al., 2019; Sayer et al., 2019; Sawyer et al., 2020), and processing of NOAA-20 data is in progress. Further, the MODIS MAIAC (Multi-Angle Implementation of Atmospheric Correction) algorithm for VIIRS is at the stage of operational integration and testing, with operational processing of both VIIRS SNPP and NOAA-20 records expected to start later in 2023. Although the VIIRS S-NPP and MODIS timeseries for both Dark Target and Deep Blue show overall consistent spatial and temporal patterns (Hsu et al., 2019; Sawyer et al., 2020; Sayer et al., 2019), comparisons between the AOD retrievals processed with Dark Target and Deep Blue for VIIRS and MODIS have shown some inevitable differences, partly influenced by factors mentioned above. Spatially the Dark Target VIIRS S-NPP AOD data exhibit an overall small positive offset almost everywhere compared to MODIS Agua (average + 0.03 for 2015), however the offset is not consistent and varies seasonally, regionally, and by wavelength (Sawyer et al., 2020). Deep Blue AOD from VIIRS S-NPP compared to MODIS shows the largest spatial differences as positive offsets over the Sahara,

Arabian Peninsula, Central Africa, Indo-Gangetic Plain, and Taklamakan Desert, due to the corresponding updates to aerosol and surface models that were implemented in the VIIRS S-NPP Deep Blue algorithm but have not yet made it into the MODIS Deep Blue algorithm (Sayer et al., 2019). The offset between the Dark Target VIIRS S-NPP time-series and MODIS Aqua is smaller than that between MODIS Terra and Aqua (Sawyer et al., 2020). The effects of these AOD differences on the PM_{2.5} record warrants attention.

In this work we examine the impact of the addition or loss of satellite AOD data sources on global geophysical-hybrid $PM_{2.5}$ estimation, and how transitioning from MODIS to VIIRS S-NPP products will affect the long-term record. We consider various scenarios where we add or remove sources to assess their importance for overall consistency in the long-term $PM_{2.5}$ record. We examine both the geophysical (calculated from satellite AOD and simulation) and hybrid (after calibration with ground monitor data) $PM_{2.5}$ estimates to examine how statistical fusion with ground monitors may help overcome differences due to the addition and removal of satellite AOD sources.

2. Methods

2.1. Satellite AOD data sources

Table S1 provides a summary of all satellite AOD sources used in our analysis. We use AOD retrieved from measurements of five satellite instruments: twin MODIS instruments, MISR, SeaWiFS, and VIIRS S-NPP.

The twin MODIS instruments have flown on the Terra and Aqua satellites since 2000 and 2002 respectively. Terra has an equator crossing time of 10:30 local time and Aqua has a crossing time of 13:30. Both MODIS instruments have spectral ranges of 0.41 μ m to 14.5 μ m and swath widths of 2330 km allowing for near-daily global coverage at the Equator and overlap of consecutive orbits at mid- and high-latitudes. We use AOD retrieved from three retrieval algorithms that process MODIS measured radiances: the current Collection 6.1 (C6.1) Dark Target (DT) and Deep Blue (DB) algorithms, and MAIAC.

The C6.1 DT retrieval algorithm (Gupta et al., 2016) performs a simultaneous inversion of two visible (0.47 μm and 0.66 μm) and one shortwave IR (2.12 μ m) channel to retrieve AOD over dark surfaces (i.e. vegetated land surfaces and dark soils). The C6.1 Dark Target algorithm includes an improved surface reflectance scheme to improve biases over urban areas, as city surfaces do not behave as a "dark" vegetated target (Gupta et al., 2016). The C6.1 DB retrieval algorithm (Hsu et al., 2019) uses blue wavelength measurements at 0.41 µm where the surface reflectance over land tends to be much lower than at longer wavelengths (typically desert surfaces). Like DT, DB also uses visible bands over vegetation, allowing for the retrieval of aerosol properties over both bright and dark surfaces. The MODIS C6.1 algorithm includes a new smoke mask that was developed based on the spectral curvature of measured reflectance to distinguish biomass burning smoke from weakly absorbing urban/industrial aerosols (Hsu et al., 2019). MODIS C6.1 DB and DT are both reported at a wavelength of 550 nm and a spatial resolution of 10 km at nadir.

The MAIAC C6 algorithm (Lyapustin et al., 2018) retrieves aerosol information at 470 nm over both bright and dark land surfaces simultaneously with surface bidirectional reflectance using time-series analysis of MODIS L1B data for up to 16 days. The prior knowledge of surface properties helps to overcome the empirical assumptions in other standard algorithms. MAIAC C6 processes the MODIS Terra and Aqua sensors jointly, which significantly increases the observation frequency required for accurate surface characterization. MAIAC C6 includes improved aerosol retrieval over bright deserts, improved cloud and snow mask, added aerosol retrievals and atmospheric correction over inland, coastal, and open ocean water, and has undergone considerable changes for global application (Martins et al., 2017). MAIAC provides AOD at a fine spatial resolution of 1 km globally over the land and coastal ocean for the entire MODIS record. The MAIAC AOD from VIIRS

will have spatial resolution of 750 m.

The MISR instrument is onboard the Terra satellite alongside MODIS. MISR observes the earth at nine different viewing angles and four spectral bands (446, 558, 672, and 866 nm) with a swath of 380 km that provides global coverage about once per week, every nine days at the equator and up to every two days near the poles (Diner et al., 1998). The MISR v23 (Garay et al., 2017, 2020) retrieval algorithm uses same-scene multi-angle views provided by the nine cameras to solve for surface and top-of-atmosphere reflectance contributions, providing AOD retrievals over bright and dark land surfaces without absolute surface reflectance assumptions (Martonchik et al., 2009). MISR retrievals use multiple aerosol models with different refractive index, particle size and shape (nonsphericity), allowing for retrieval of aerosol size and type in many conditions. MISRv23 reports AOD at 550 nm at a spatial resolution of 4.4 km.

The SeaWiFS instrument flew on the SeaStar satellite which had a noon overpass time and was operational between 1997 and 2010. SeaWiFS maintained highly accurate and stable calibration over its lifetime (Sayer et al., 2012). SeaWiFS provided measurements in eight spectral bands between 412 and 885 nm and had a 1500 km swath width that provided nearly daily global coverage. We use AOD retrieved from the version 4 SeaWiFS Deep Blue (Sayer et al., 2012) dataset that offers AOD at a wavelength of 550 nm and a spatial resolution of 13.5 km.

Two VIIRS instruments are currently in orbit, aboard the S-NPP since 2011 and the Joint Polar Satellite System-1 (JPSS-1: in operation as NOAA-20) since 2017. VIIRS NOAA-20 AOD data were not accessible to us at the time of this work, so we consider only the VIIRS S-NPP data.

The S-NPP satellite has an overpass time of ~13:30, similar to Aqua, however the two satellites orbit at different altitudes (824 km for VIIRS S-NPP, 750 km for MODIS Aqua). The VIIRS instrument was designed to have similar capabilities as MODIS in terms of spectral channels and spatial coverage; however, there are some key differences, such as slightly different center wavelengths, the larger swath width (3040 km vs 2330 km) of VIIRS, and the finer DT and DB product resolution at nadir (6 km vs 10 km) of VIIRS. On-board detector aggregation of VIIRS reduces the "bow-tie" distortion (pixels away from nadir views become larger and consecutive scans begin to overlap) that exist in MODIS retrievals, despite the broader swath width of VIIRS (Wolfe et al., 2013). We use AOD from two retrieval algorithms processing VIIRS measured radiances: Dark Target and VIIRS Deep Blue V1. Both algorithms were ported to process VIIRS radiances by the teams behind their MODIS counterparts. As a result, both algorithms are conceptually the same as the MODIS C6.1 versions. The differences in spectral bands between VIIRS and MODIS leads to a slight difference in the bands used for both the MODIS C6.1 Dark Target and C6.1 Deep Blue algorithms, and results in a difference in the cloud mask used in VIIRS Dark Target vs MODIS C6.1 Dark Target. The VIIRS Deep Blue V1 algorithm includes updates to the aerosol and surface models used in the retrieval that did not make it into the release of MODIS C6.1 Deep Blue (Sayer et al., 2019).

2.2. GEOS-Chem simulation

We use the GEOS-Chem chemical transport model originally described by Bey et al. (2001), v11–01 as a data source for AOD and to represent the relationship of surface $PM_{2.5}$ to total column AOD (described in section 2.3). A detailed description of the simulation is given in Hammer et al. (2020). The GEOS-Chem model solves for the evolution of atmospheric aerosols and gases using a detailed oxidant-aerosol chemical mechanism, emission inventories, and assimilated meteorological data. The assimilated meteorological data are from the Modern-Era Retrospective analysis for Research and Applications, Version 2 (MERRA-2) Reanalysis of the NASA Global Modeling and Assimilation Office (Gelaro et al., 2017). We conduct our simulations for 1998–2019. We use the global spatial resolution of $2^{\circ} \times 2.5^{\circ}$ and the nested spatial resolution of $0.5^{\circ} \times 0.625^{\circ}$ over North America, Europe, and Asia with 47 vertical layers. The top of the lowest model layer is

~100 m. Regional anthropogenic emission inventories of aerosols and their precursors are used over the United States [EPA/NEI11 (Travis et al., 2016)], Canada (CAC; http://www.ec.gc.ca/pdb/cac/), Mexico [BRAVO (Kuhns et al., 2005)], Europe (EMEP; http://www.emep.int/), China [MEIC (Li et al., 2017)], India (Lu et al., 2011), and elsewhere in Asia [MIX (Li et al., 2017)].

2.3. Algorithm for estimating PM_{2.5} concentrations from satellites, simulation, and ground monitors (V4.GL.03)

We follow the V4.GL.03 algorithm from Hammer et al. (2020) for calculating the geophysical and geophysical-hybrid (denoted hybrid) $PM_{2.5}$ estimates and summarize the algorithm here. The resulting estimates are produced for 1998 to 2019 at a spatial resolution of 5 km for the geophysical $PM_{2.5}$ estimates and 1 km for the hybrid estimates.

2.3.1. Geophysical PM_{2.5} estimates

We first combine the satellite AOD products, and for this work consider several different scenarios where satellite AOD sources were either included or excluded (described in Section 3). The various satellite AOD sources are combined based on their relative uncertainties with the global sun photometer network Aerosol Robotic NETwork (AERO-NET) V3 (Giles et al., 2019), which provides AOD measurements with high accuracy (uncertainty <0.02). Simulated AOD from GEOS-Chem is also used as an additional AOD source; however, its contributions are mostly over snow- and ice-covered northern regions where and when satellite retrievals are sparse. Hammer et al. (2020) found that satellite retrievals comprised 81% of the population-weighted AOD contribution for 1998 to 2018. The different sources of error associated with satellite and simulated AOD require care in accounting for their relative uncertainties. Briefly, one of the main sources of uncertainty associated with satellite retrieved AOD is the surface treatment used in the retrieval, which we assess by comparison with AERONET as a function of land type. For the simulated AOD, to account for errors due to speciesspecific emissions and assumed aerosol microphysical properties, we calculate the relative uncertainty based on the simulated fractional aerosol composition applied to each daily AERONET observation following van Donkelaar et al. (2016).

To estimate surface concentrations of $PM_{2.5}$ ($PM_{2.5,SAT}$) from satellite AOD (AOD_{SAT}), we use the local, coincident ratio (η) of simulated surface $PM_{2.5}$ concentrations ($PM_{2.5,SIM}$) to simulated total column AOD (AOD_{SIM}):

$$PM_{2.5} = \eta \times AOD_{SAT}$$
 (1)

where

$$\eta = \frac{PM_{2.5,SIM}}{AOD_{SIM}} \tag{2}$$

 η is a function of the factors that relate $PM_{2.5}$ mass to satellite AOD (e.g., aerosol size, aerosol composition, diel variation, relative humidity, and the vertical structure of aerosol extinction (van Donkelaar et al., 2006). To account for differences in temporal sampling of the AOD data sources, we calculate daily values of η as the ratio of 24-h surface $PM_{2.5}$ at a relative humidity of 35%, to total-column AOD at ambient relative humidity sampled at satellite overpass time. We address the sampling limitations of satellite AOD in the presence of snow or cloud cover by using GEOS-Chem to scale the satellite AOD by the ratio of simulated monthly mean AOD to simulated AOD coincident with satellite AOD as described in Hammer et al. (2021).

2.3.2. Geophysical-hybrid (denoted "hybrid") $PM_{2.5}$ estimates

We use geographically weighted regression (GWR) (Brunsdon et al., 1998; Fotheringham et al., 1998) to predict and account for the bias in the annual mean geophysical $PM_{2.5}$ estimates as described by van Donkelaar et al. (2016). GWR is an extension of least-squares regression

that allows predictor coefficients to vary spatially by weighting the estimate- observation pairs at multiple geographic locations according to their inverse squared distance from individual observation sites. The GWR is conducted at a 1-km resolution to calibrate annual predictor coefficients based on comparison with coincident ground monitor observations. We use monitor-specific ground-based measurements of PM_{2.5} from an updated version of the WHO Global Ambient Air Quality Database (World Health Organization, 2018). This database consolidates observations provided by, and according to the standards of, numerous national, regional and international agencies. These include agencies and networks operating in countries around the world, as well as data provided by the European Environment Agency, the Surface Particulate Matter Network (SPARTAN) network, globally installed embassy-based monitors operated by the United States Environmental Protection Agency, Clean Air Asia, OpenAQ, among others. The predictors used in the GWR calculation are the log of the elevation difference between the local elevation and the mean elevation within the simulation grid cell, the inverse distance to the nearest urban land surface, and the simulated relative contributions of mineral dust and the sum of sulfate, nitrate, ammonium, and organic carbon. The bias predicted by the GWR is used to adjust the geophysical PM2.5 estimates to produce the hybrid PM_{2.5} estimates.

2.3.3. Analysis scenarios adding and removing satellite AOD sources from geophysical-hybrid $PM_{2.5}$

Table 1 contains the scenarios where satellite AOD sources are added or removed to analyze the impact on geophysical and hybrid $PM_{2.5}$ estimates. Hammer et al. (2020) found that MODIS MAIAC made the largest contribution overall to hybrid $PM_{2.5}$ estimates, but as VIIRS S-NPP MAIAC is not yet available, we do not include MODIS MAIAC in our main analysis. A separate analysis including MODIS MAIAC is in the Appendix. Table A1 describes the scenarios when including MAIAC.

Each scenario is calculated following the algorithm described in Section 2.3. The "Base" scenario uses the Hammer et al. (2020) V4.GL.03 algorithm excluding MAIAC. The scenario denoted "wVIIRS" adds the VIIRS S-NPP Dark Target and Deep Blue products to the Base scenario for the VIIRS record (for 2012-onward). The other scenarios are designed to examine the impact on geophysical and hybrid PM_{2.5} estimates as more sources are removed until only the VIIRS and GEOS-Chem AOD remain. The wVIIRS_noMODISDBDT scenario is based on wVIIRS, but MODIS Deep Blue and Dark Target for both Terra and Aqua are removed from 2012-onward. The wVIIRS_noMODISTerra scenario is based on wVIIRS, but all MODIS Terra products (Deep Blue and Dark Target from just Terra) are removed from 2012-onward. The wVIIRS_noTerra scenario is the same as wVIIRS, but MODIS Terra and MISR are removed from 2012-

Table 1The geophysical-hybrid PM_{2.5} scenarios.

Scenario	Description
Base	Based on V4.GL.03 algorithm: includes MODIS Deep Blue and Dark Target from Terra (2000 to 2019) and Aqua (2002 to 2019), MISR (2000 to 2019), SeaWiFS (1997 to
wVIIRS	2010) and GEOS-Chem simulated AOD Base scenario with the addition of VIIRS Deep Blue and
wVIIRS_noMODISDBDT	Dark Target for the VIIRS record (2012 to 2019) (to evaluate the impact of adding VIIRS to the Base Case) wVIIRS scenario with the MODIS Deep Blue and Dark
wVIIRS noMODISTerra	Target products from both Terra and Aqua removed (to evalulate the impact of the loss of retrieval algorithms) wVIIRS scenario with all MODIS product from Terra
wvinto_nomobioTerra	removed (MODIS Deep Blue and Dark Target) (to evaluate the loss of an instrument)
wVIIRS_noTerra	wVIIRS scenario with all Terra products removed (MODIS Deep Blue, Dark Target, and MISR) (to evaluate the loss of
justVIIRS	a satellite) Scenario including just VIIRS Deep Blue, Dark Target, and GEOS-Chem simulated AOD (to evaluate the loss of all
	Terra/Aqua products)

onward. The wVIIRS_noMODISDBDT, wVIIRS_noMODISTerra, and wVIIRS_noTerra scenarios allow examining the relative impacts of loss of an instrument, algorithm, or satellite. The justVIIRS scenario only includes VIIRS S-NPP Dark Target and Deep Blue for 2012-onward.

3. Results and discussion

3.1. Impact of satellite AOD source addition and removal on geophysical PM_{2} s

The top panel of Fig. 1 shows the Base scenario 2012 to 2019 mean geophysical PM_{2.5}, whereas the top panel of Fig. A1 shows the same but when including MAIAC. Most of the world exhibits mean concentrations between 5 and 30 μ g/m³, but there are elevated concentrations between 50 and 90 μ g/m³ over parts of China, India, the Middle-East and northern Africa. The geophysical 2012 to 2019 mean values are very similar for the case when including MAIAC (Fig. A1).

Fig. 2 shows the absolute differences between the 2012 to 2019 mean geophysical $PM_{2.5}$ concentrations for each scenario in Table 1 and the Base scenario (top panel of Fig. 1). Fig. S1 shows the same but in percent difference, which exhibit similar spatial patterns as Fig. 2. Fig. S2 shows the absolute differences for combined AOD. PM_{2.5} concentrations exhibit increases between 5 and 20 µg/m³ over most desert regions and decreases between -20 and $-5 \mu g/m^3$ over parts of China, India, and Iran. For each scenario, the patterns of geophysical PM_{2.5} change and of combined AOD change with respect to the Base scenario are similar to one another (Pearson's correlation coefficient r = 0.77 to 0.86). Most differences in AOD and PM25 occur in regions with sparse AERONET coverage, which explains why the bias correction in our algorithm for combining each separate AOD source (which is calculated based on the uncertainty compared to AERONET) does not eliminate all differences when sources are added or removed. Increases in annual $PM_{2.5}$ between 10 and 20 μg/m³ are apparent over Indonesia, despite decreases in annual combined AOD (Fig. S2). Figs. S3 and S4 show the absolute differences for geophysical PM2.5 and combined AOD respectively zoomed in for Indonesia. These conflicting differences reflect the increased AOD, η , and PM_{2.5} during months with biomass burning that drive the annual mean PM_{2.5} in the region. Peat fires in Indonesia occur later in the year, and the strength of the fires is influenced by years with particularly strong El Niño (Sayer et al., 2019).

The magnitude of differences in PM_{2.5} in Fig. 2 is smallest for wVIIRS-Base and largest for justVIIRS-Base. The wVIIRS noMODISTerra and wVIIRS noTerra differences are very similar (global r=0.95, RMSD = 1.03 µg/m³). The wVIIRS noMODISDBDT-Base and justVIIRS-Base are similar (global r=0.88, RMSD = 1.03 µg/m³). The larger differences for the latter case (two-sample Kolmogorov-Smirnov test, p<0.05) indicate that the loss of MODIS products in general has a larger impact than the loss of a single satellite or algorithm.

Fig. A2 shows the same as Fig. 2 but for the analysis when including MAIAC AOD in the scenarios. The spatial pattern of differences is similar to the no MAIAC scenarios (global r=0.80 to 0.89, RMSD =1.5 to 1.7 µg/m³), however the decreases in PM_{2.5} over China and India are further emphasized by changes whether MAIAC is included or excluded.

Fig. S5 shows the mean contribution of each AOD data source to the wVIIRS scenario for 2012 to 2019 to aid in the interpretation of Fig. 2. The increases over desert regions correspond to regions where VIIRS Deep Blue and MODIS Deep Blue have the highest weightings of all sources. The decreases over China, India, and Iran correspond to regions where VIIRS Deep Blue has the highest weightings. Simulated weightings are higher in Fig. S5 than in Hammer et al. (2020) due to the exclusion of MAIAC from Fig. S5.

The differences between satellite AOD products before they are incorporated into our algorithm also offer insight into the differences in Fig. 2. Fig. 3 shows the absolute differences between the 2012 to 2019 mean of the VIIRS S-NPP AOD products (SatVIIRS; includes VIIRS Deep Blue and Dark Target) and the 2012 to 2019 mean of the AOD products

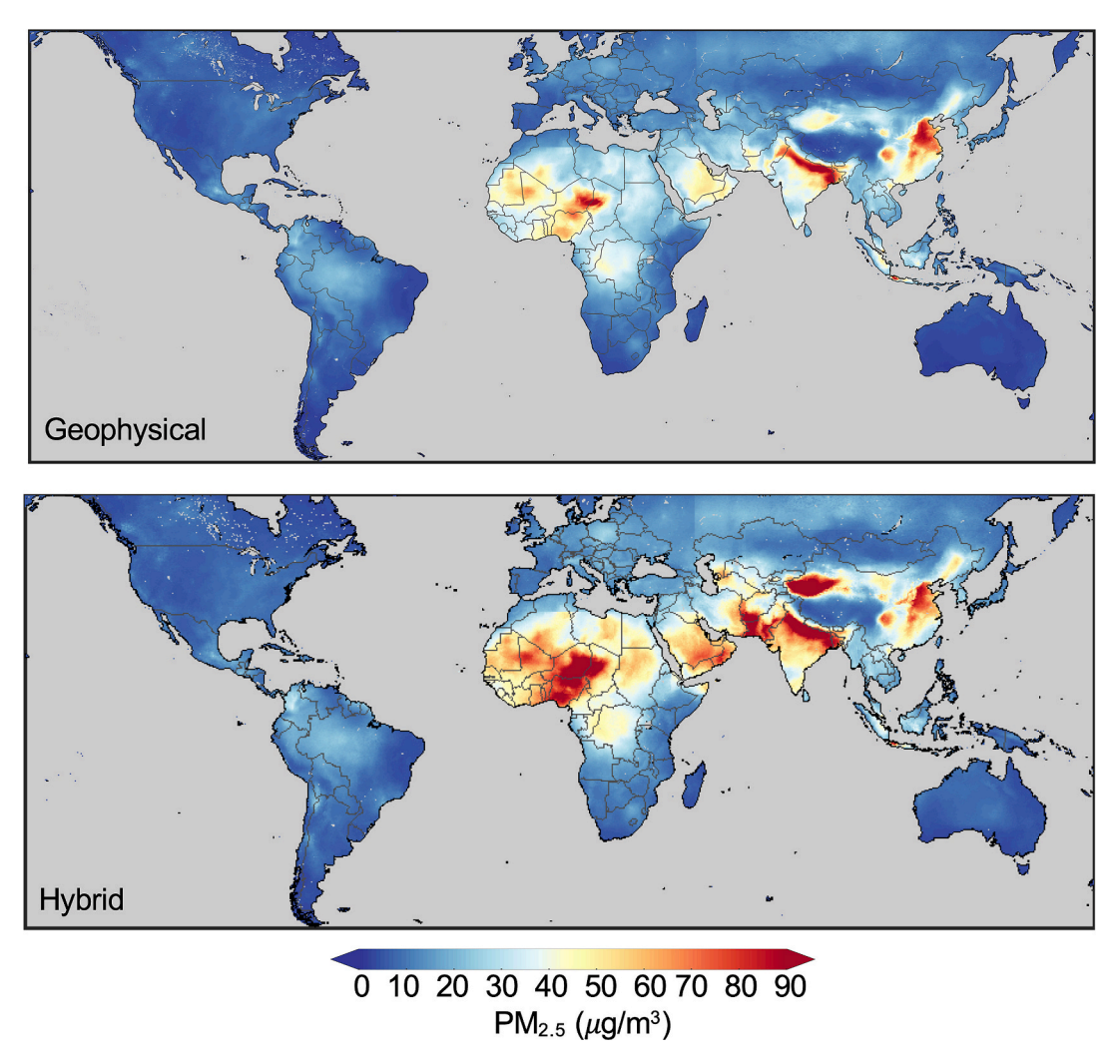


Fig. 1. The Base scenario mean PM_{2.5} concentrations for 2012 to 2019. The top panel shows the geophysical values while the bottom panel shows the hybrid values. Grey indicates missing data or water.

used in our Base scenario (SatM; includes MODIS Terra/Aqua Deep Blue and Dark Target, and MISR). Fig. S6 shows the same but for percent differences, which exhibit similar spatial patterns as Fig. 3 albeit with some larger ratios in regions with low AOD such as in Australia. The top panel of Fig. 3 shows the differences when all valid pixels are included (All valid pixels) and the bottom panel shows the differences when only pixels that are coincidently sampled between all sources are included (Coincidently sampled). The most notable features are increases in SatVIIRS AOD compared to SatM AOD of ~0.2 over desert regions (i.e. the Sahara, parts of the Middle-East, parts of Australia, Taklamakan), similar to the increases in geophysical PM_{2.5} seen in Fig. 2. These increases are similar irrespective of whether sampling is considered. Sayer et al. (2019) evaluated the differences between VIIRS S-NPP Deep Blue and the MODIS Deep Blue products and found similar increases which were explained by aerosol model and surface treatment updates that were included in the VIIRS Deep Blue algorithm but not in the MODIS C6.1 Deep Blue algorithm (as the VIIRS algorithm was more recent than the C6.1 MODIS reprocessing). Specifically, new nonspherical dust optical models (Lee et al., 2017) were introduced in the V1 VIIRS Deep Blue to improve AOD retrievals over deserts including the Sahara, Arabian Peninsula, and Taklamakan desert. The dust models generally resulted in higher AOD, as depicted in Fig. 3. The increases over the Thar desert and part of Australia were found to be partly due to slight differences in surface treatment as well. As the increases in AOD were more than intended, the Deep Blue team has made further improvements in

both dust optical models and surface reflectances in the V2 algorithm, which will decrease the gap between MODIS and VIIRS, while maintaining better observation geometry dependence of dust AOD resulting from more realistic representation of nonspherical dust. These algorithmic differences correspond to the increases observed over desert regions in Fig. 2.

In the "All valid pixels" case of Fig. 3 there are decreases between -0.1 and -0.05 over parts of China, the Indo-Gangetic Plain, Indonesia, Iran, and central Africa that are not apparent in the coincidently sampled case indicating the role of sampling differences between the instruments and algorithms in contributing to differences in Fig. 2. The decrease in AOD over Indonesia in the "All valid pixels case" demonstrates that the decrease in combined AOD over the region in Fig. S2 is at least partially due to sampling. There are small increases (<0.05) over Canada and northern Brazil that are smaller in magnitude for the coincidently sampled case, that are not apparent in the geophysical PM2.5 differences in Fig. 2. Sampling plays a larger role in areas affected by pronounced temporal differences (such as Canada, Brazil, and Indonesia). Fig. A3 shows the same as Fig. 3 but includes MAIAC AOD in SatM. The spatial pattern of differences is similar; however, including MAIAC causes sampling differences that partially mask the increases between VIIRS Deep Blue and MODIS C6.1 Deep Blue AOD over deserts and causes decreases between -0.15 and -0.05 over many parts of the world.

Fig. 4 shows scatterplots of geophysical PM_{2.5} for each scenario from

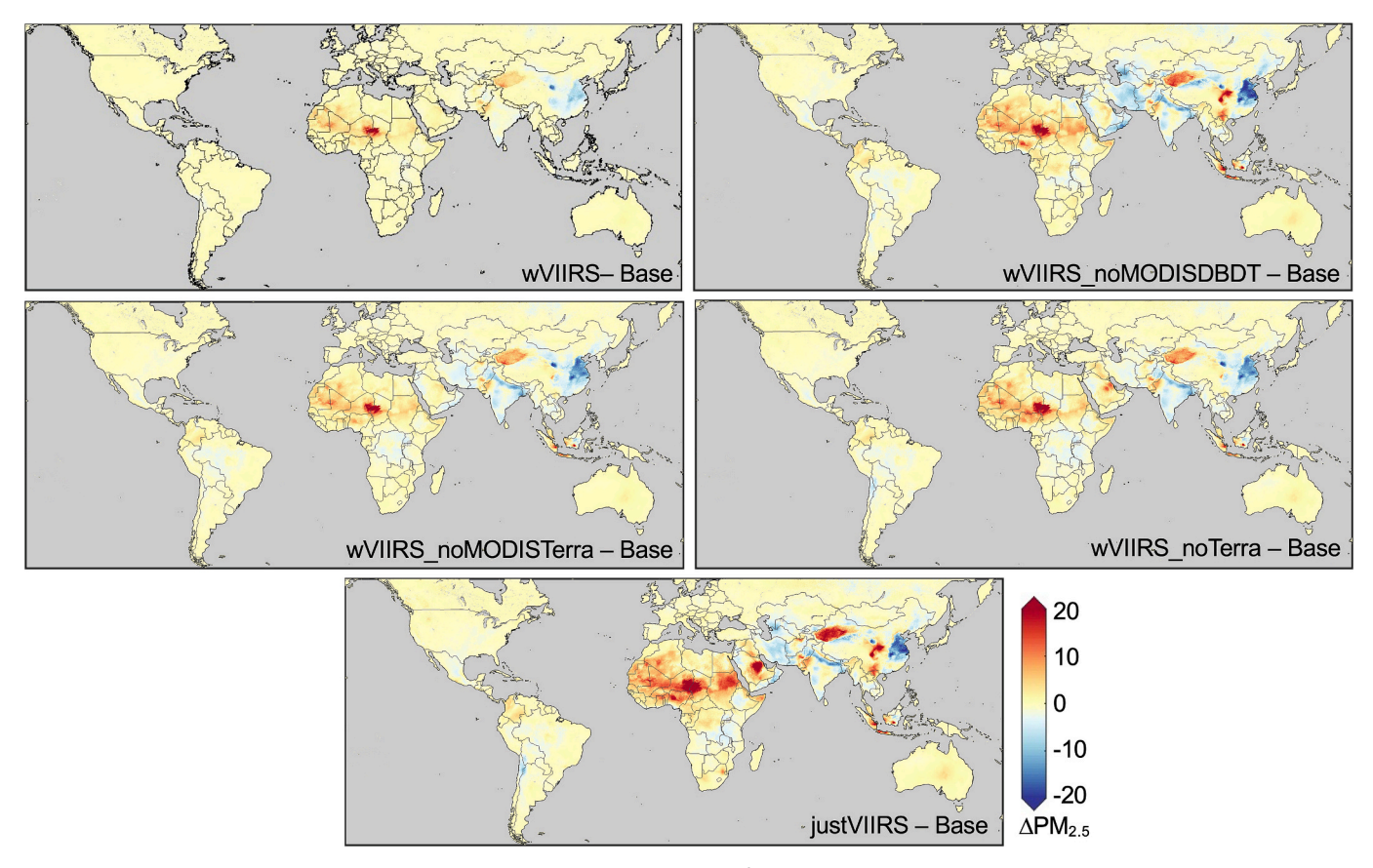


Fig. 2. The difference in the 2012 to 2019 mean geophysical $PM_{2.5}$ concentrations ($\mu g/m^3$) between each scenario from Table 1 and the Base scenario. Grey indicates missing data or water.

Table 1 vs ground monitor data. All scenarios have similar coefficients of determination ($R^2=0.79$ to 0.81). Introducing the VIIRS products slightly improves correlation compared to the Base scenario, but also decreases the slope, with the slope further decreasing as sources are removed. The decreases in slope reflect the decreases over China apparent in Fig. 2, driven by sampling differences of valid retrievals using current algorithms as evident in Fig. 3. Fig. S7 shows a comparison of the combined AOD for each scenario and AERONET AOD, giving similar agreement as Fig. 4 ($R^2=0.76$ to 0.80). Fig. A4 shows similar comparisons to Fig. 4 but including MAIAC AOD in the scenarios. Including MAIAC increases the slopes for the scenarios that include MAIAC indicating the value of MAIAC AOD for PM_{2.5} estimates at high concentrations.

3.2. Impacts of source addition and removal on trends in geophysical $PM_{2.5}$

We examine how the addition or removal of satellite sources affects trends or discontinuities. Fig. 5 shows the 1998–2019 trends in geophysical PM_{2.5} for the Base scenario, the wVIIRS scenario, and the justVIIRS scenario. We show trends over the 1998 to 2019 period to demonstrate the impacts of source addition and removal on the entire record of our PM_{2.5} datasets. The spatial pattern of trends is broadly similar between scenarios, with the most noticeable difference being statistically significant (*p*-value <0.05) positive trends (1.0 to 1.5 μ g m⁻³ yr⁻¹) that appear over the Sahara in the wVIIRS and justVIIRS scenarios. There are also statistically significant positive trends (<0.25 μ g m⁻³ yr⁻¹) that appear over Australia most noticeably in the justVIIRS scenario. All three scenarios show statistically significant negative trends over the eastern United States (-0.5 to -0.25 μ g m⁻³ yr⁻¹), Brazil (-0.1 to -0.25 μ g m⁻³ yr⁻¹), Europe (-0.5 to -0.25 μ g m⁻³ yr⁻¹), and

central China (< $-1.5~\mu g~m^{-3}~yr^{-1}$), and statistically significant positive trends over Saudi Arabia, Yemen, and Oman (1 to 1.5 $\mu g~m^{-3}~yr^{-1}$), India (0.5 to 1.5 $\mu g~m^{-3}~yr^{-1}$), and the Taklamakan Desert (1.0 to 1.5 $\mu g~m^{-3}~yr^{-1}$).

Fig. 6 shows the 1998 to 2019 population-weighted timeseries for each scenario from Table 1 for each of the six regions outlined with black boxes in the top panel of Fig. 5. Population estimates are from the Gridded Population of the World (GPW v4) database (CIESIN (Center for International Earth Science Information Network), 2017). Populationweighted mean PM_{2.5} values are calculated as a weighted average weighted by the population estimates for the same year. The timeseries generally maintain consistency between scenarios in all regions. The largest variations are in the timeseries for the SAH (Sahara and Middle East) region. The larger within-region variability in Fig. 5 than in the timeseries of Fig. 6 reflects that Fig. 6 represents population-weighted averages over the domain. Table 2 shows the mean offset between the 2012 to 2019 regional timeseries for each scenario and the Base scenario. Overall the variation in magnitude of offsets between scenarios is small, ranging between -10.28% and 1.86% of local 2012 to 2019 mean Base scenario values, with differences related to algorithmic changes as described above.

Table 3 shows the population-weighted 1998 to 2019 trend slopes with standard error for each scenario and region. The trends across scenarios show mostly small variations that are within the standard error values for most regions.

3.3. Impact of satellite AOD source addition and removal on hybrid $PM_{2.5}$

The bottom panel of Fig. 1 shows the Base scenario 2012 to 2019 mean hybrid PM_{2.5}, while the bottom panel of Fig. A1 shows the same but when including MAIAC. The mean hybrid PM_{2.5} concentrations are

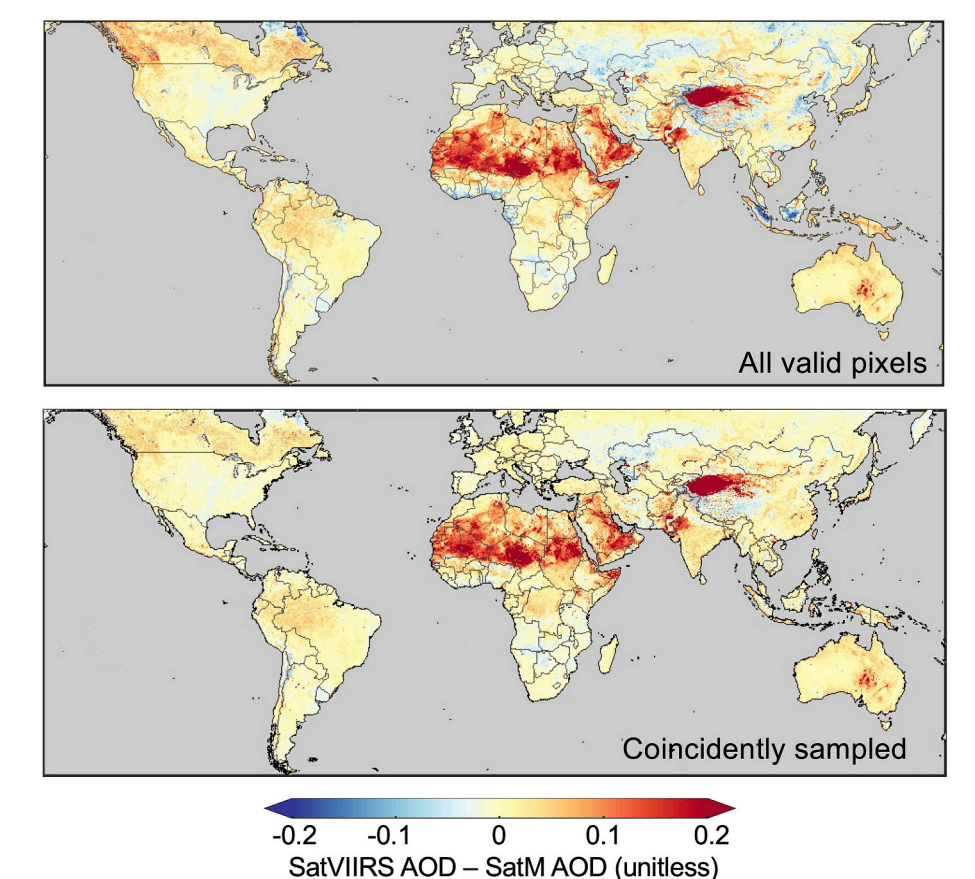


Fig. 3. Difference between the mean SatVIIRS AOD and the mean SatM AOD for 2012 to 2019. The SatVIIRS AOD includes VIIRS S-NPP Dark Target and Deep Blue, while SatM AOD includes MODIS Deep Blue and Dark Target from both Terra and Aqua, and MISR. For the top panel the means were calculated for all valid pixels and for the bottom panel the means only include coincidently sampled pixels between all products. Grey indicates missing data or water. (For interpretation of the references to color in this figure legend, the reader is referred to the web version of this article.)

similar to the geophysical, with further enhancements of concentrations over parts of China, India, and the Sahara, that are very similar when including MAIAC (Fig. A1). The particularly high enhancements over northern Africa and India are due mainly to predicted increases in mineral dust (Hammer et al., 2020).

Fig. 7 shows the absolute differences between the 2012 to 2019 mean hybrid PM_{2.5} concentrations for each scenario in Table 1 and the Base scenario. Fig. S8 shows corresponding percent differences. The inclusion of the bias predicted by GWR eliminates the decreases over China and India apparent for the geophysical PM_{2.5} (Fig. 2), although it introduces some increases between 5 and 20 μg/m³ over central China. The hybrid estimates also exhibit further increases over most desert regions and further decreases over Iran. These results suggest the GWR correction helps to overcome some of the biases due to sampling differences when adding and removing satellite sources, however the exacerbated differences over desert regions reflect uncertainty in the GWR correction in regions with sparse monitoring. Improving the accuracy of the GWR correction in areas with sparse monitoring is an ongoing effort in our development of satellite-derived PM_{2.5} algorithms. The effects of different scenarios resemble Fig. 2 in that the smallest changes are for wVIIRS-Base and largest for justVIIRS-Base.

Fig. 8 shows scatterplots of hybrid $PM_{2.5}$ for each scenario from Table 1 and ground monitor data. The scatterplots show 10-fold out-of-sample 10% cross validation at sites that were not used in the GWR regression. The coefficients of determination are high for all scenarios ($R^2=0.91$ to 0.92) and all scenarios exhibit similar slopes (ranging from 1.00 to 1.02) and similar levels of scatter, indicating the combination of geophysical estimates and statistical fusion with ground monitors leads to overall accuracy and precision that is robust to AOD source addition and removal.

4. Conclusions

The ability to sustain accurate global satellite-derived PM $_{2.5}$ estimates requires assessment of how the estimates respond to discontinuities in the input satellite AOD sources. This work examines the impact of the addition or loss of satellite AOD sources on geophysical-hybrid PM $_{2.5}$ estimation and the impact of continuing the long-term record with AOD from VIIRS after the loss of the MODIS and MISR instruments on board the Terra and Aqua satellites, which is expected in the next few years.

We find that the addition of VIIRS S-NPP Dark Target and Deep Blue AOD products causes an overall increase between 5 and 20 $\mu g/m^3$ in geophysical $PM_{2.5}$ over desert regions, an increase between 10 and 20 $\mu g/m^3$ over Indonesia, and a decrease between -20 and -5 $\mu g/m^3$ over parts of China, India, and Iran. The increases in $PM_{2.5}$ over desert regions correspond to differences in the VIIRS and MODIS Deep Blue AOD algorithms noted in earlier work while the decreases over China, India, and Iran reflect sampling differences. The loss of the MODIS products in general has a larger impact than the loss of a single satellite or algorithm.

We find overall consistency in the spatial distribution of long-term trends between scenarios, and no obvious discontinuities or inconsistencies in the regional timeseries. The variation in magnitude of offsets between scenarios is small and within a small percentage of local mean Base scenario values.

Statistical fusion with ground monitor data helps to overcome some of the biases due to sampling differences when adding and removing satellite sources, particularly over China and India. However, differences over desert regions are exacerbated, reflecting the uncertainty in the GWR correction for regions with sparse monitoring. Improving our understanding and resolving some of the discrepancies between satellite retrievals in such regions is important due to the lack of ground monitor coverage. Overall the slopes (1.00 to 1.02) and coefficients of determination ($R^2=0.91$ to 0.92) of the hybrid estimates versus ground-based

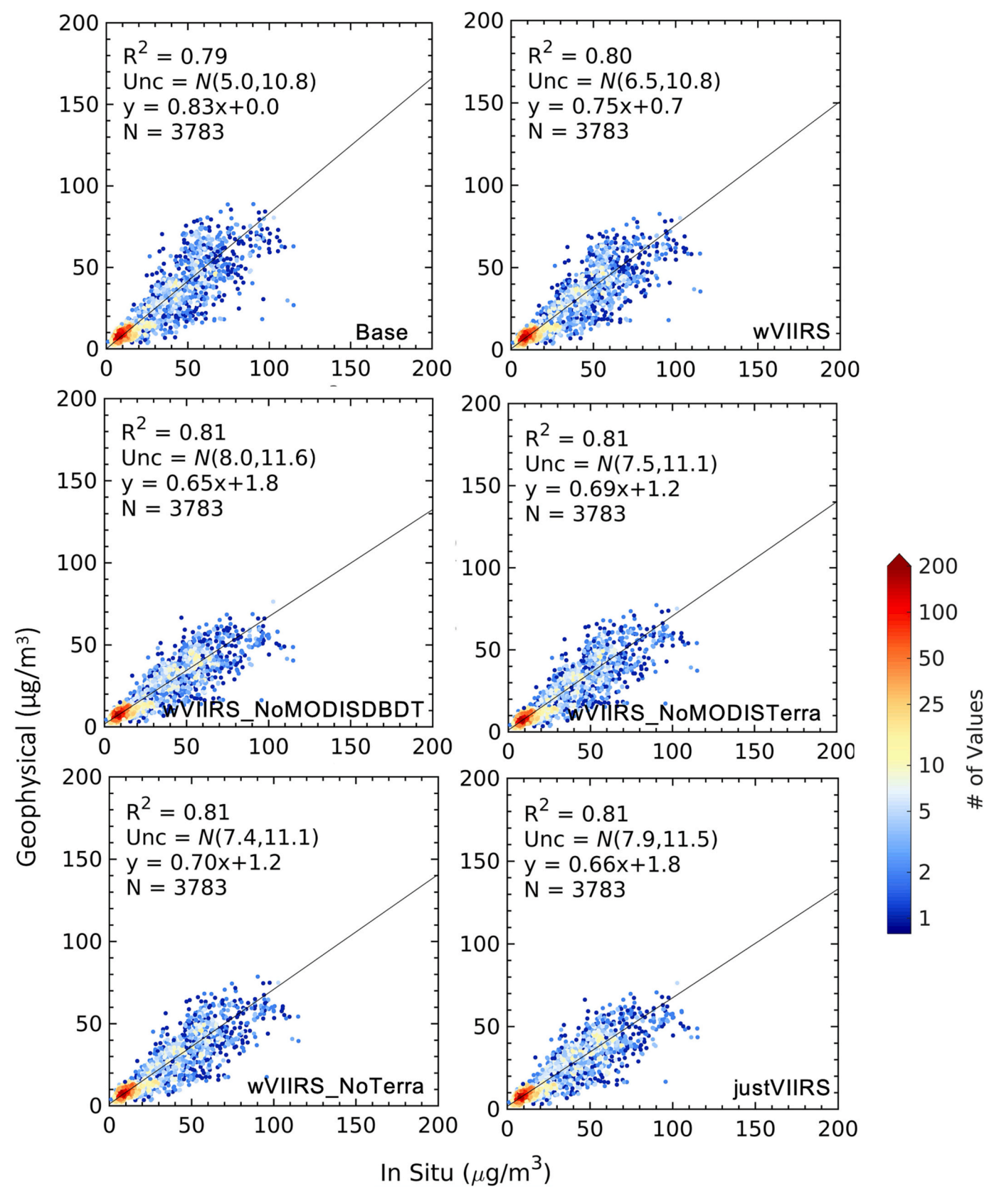


Fig. 4. Annual mean geophysical $PM_{2.5}$ concentrations for each scenario from Table 1 for 2015 versus collocated annual mean in situ values for 2015. Included on the plots are the coefficient of determination (R^2), the normal distribution of uncertainty (N(bias, variance)), the line of best fit (y) using reduced major axis linear regression, and the number of comparison points (N). The color scale indicates the number density of observations at each point.

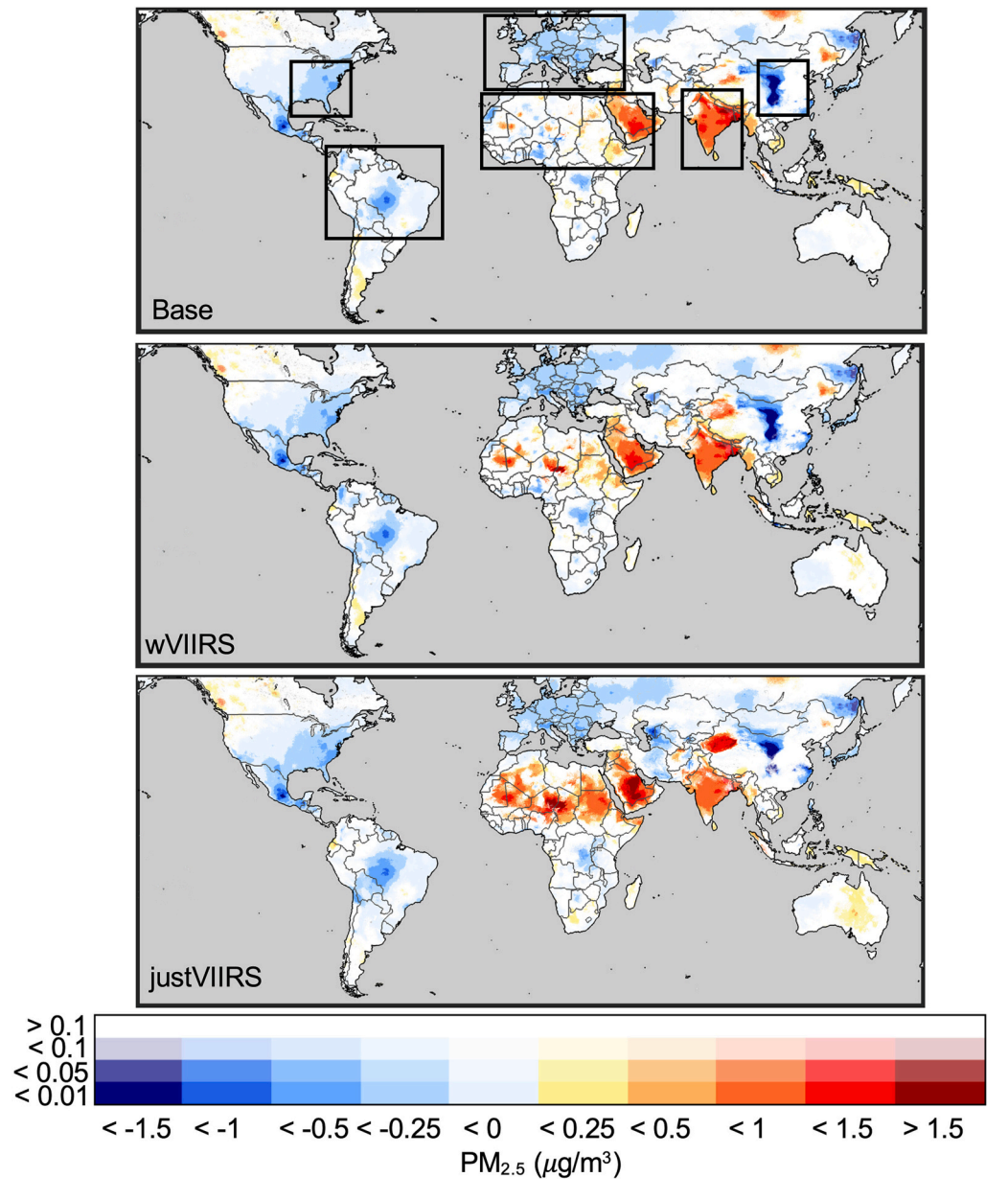


Fig. 5. Trends in geophysical $PM_{2.5}$ concentrations for 1998 to 2019 calculated from the generalized least-squares regression of monthly time series, for the Base scenario, the wVIIRS scenario, and the justVIIRS scenario. Warm colors indicate positive trends, cool colors indicate negative trends, and the opacity of the colors provides a measure of the statistical significance of the trends. Grey denotes water. Boxes indicate areas featured for regional analysis in Fig. 6.

monitors remain consistent across all scenarios indicating that the overall accuracy and precision of the hybrid estimates is robust to changes in satellite AOD sources.

In support of the upcoming MODIS Collection 7 reprocessing, the effort of backporting VIIRS DB algorithm to MODIS is already underway. This will significantly improve the DB AOD consistency between MODIS and VIIRS over desert regions. The forthcoming VIIRS V2 Deep Blue dataset as well as the VIIRS MAIAC dataset have the potential to further reduce differences in geophysical-hybrid estimates compared to using AOD products from Terra and Aqua, provided the AOD algorithms applied to VIIRS are also applied to MODIS. This work offers promise for the continued development of a consistent, long-term geophysical-hybrid PM_{2.5} dataset into the future using AOD products from VIIRS.

Author responsibilities

MSH, AVD, and RVM designed the study. MSH produced the

satellite-derived $PM_{2.5}$ estimates, conducted the analysis of all data, and compiled all figures. MSH, AVD, and RVM wrote the manuscript with contributions from all coauthors. LB contributed to the development of the GEOS-Chem simulations used. AL, AMS, NCH, VS, RCL, MJG, OVK, RAK produced the satellite AOD products.

Funding sources

This work was supported by NASA (grant number 80NSSC22K0200), by the Energy Policy Institute at the University of Chicago, and by Washington University in St. Louis.

Declaration of Competing Interest

The authors declare that they have no known competing financial interests or personal relationships that could have appeared to influence the work reported in this paper.

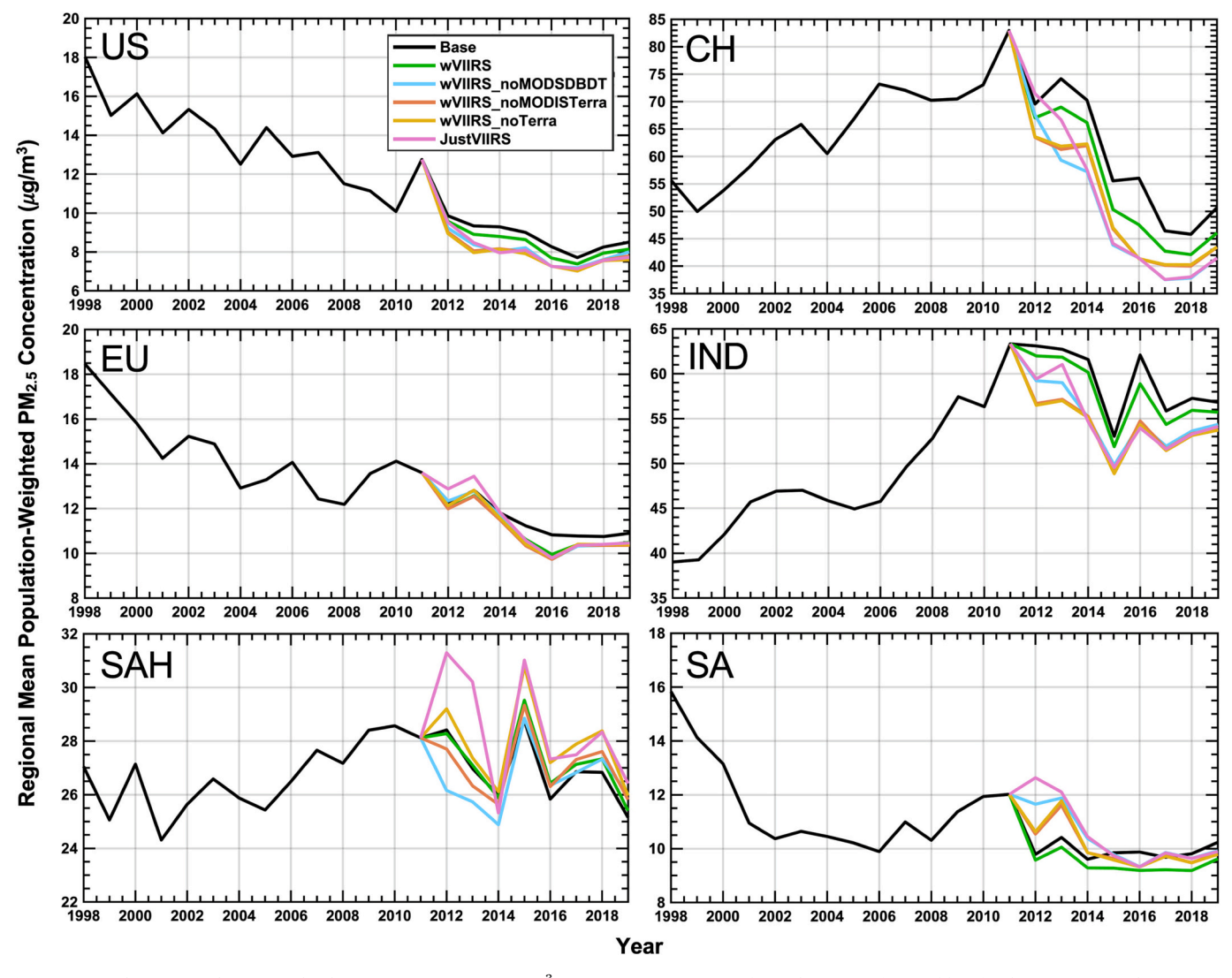


Fig. 6. Regional mean population-weighted PM_{2.5} concentration (μg m⁻³) 1998 to 2019 timeseries for each scenario from Table 1 for the eastern United States (US), China (CH), Europe (EU), India (IND), Sahara + Middle East (SAH), and northern South America (SA).

Table 2 The regional population-weighted mean offset ($\mu g \ m^{-3}$) between the 2012 to 2019 timeseries for each scenario from Table 1 and the Base scenario timeseries. The variation in offsets between scenarios for each region is given as the percentage of the 2012 to 2019 mean Base scenario values (% of local mean).

Scenario	US	СН	EU	IND	SAH	SA
wVIIRS	-0.05	-1.32	-0.02	1.30	0.32	0.54
wVIIRS_NoMODISDBDT	-0.70	-9.13	-0.35	-3.89	-0.30	0.35
wVIIRS_NoMODISTerra	-0.81	-7.78	-0.46	-4.53	0.14	0.08
wVIIRS_NoTerra	-0.87	-7.59	-0.38	-4.71	0.90	0.09
JustVIIRS	-0.72	-7.79	-0.17	-3.87	1.40	0.48
% local mean	-6.34%	-10.28%	-2.49%	-4.76%	1.68%	1.86%

Table 3 The regional population-weighted 1998 to 2019 trend slope \pm standard error ($\mu g \ m^{-3} \ yr^{-1}$) for each scenario from Table 1.

Scenario	US	СН	EU	IND	SAH	SA
Base	-0.43 ± 0.03	-0.17 ± 0.63	-0.29 ± 0.03	0.98 ± 0.23	0.05 ± 0.04	-0.19 ± 0.06
wVIIRS	-0.44 ± 0.02	-0.32 ± 0.65	-0.31 ± 0.05	1.03 ± 0.25	0.08 ± 0.04	-0.17 ± 0.06
wVIIRS_NoMODISDBDT	-0.48 ± 0.03	-0.70 ± 0.74	-0.32 ± 0.03	0.75 ± 0.27	0.05 ± 0.04	-0.19 ± 0.07
wVIIRS_NoMODISTerra	-0.49 ± 0.04	-0.61 ± 0.71	-0.32 ± 0.03	0.72 ± 0.25	0.07 ± 0.04	-0.20 ± 0.06
wVIIRS_NoTerra	-0.49 ± 0.04	-0.60 ± 0.71	-0.32 ± 0.03	0.71 ± 0.25	0.11 ± 0.05	-0.20 ± 0.06
JustVIIRS	-0.48 ± 0.03	-0.68 ± 0.75	-0.32 ± 0.05	0.74 ± 0.28	$\textbf{0.14} \pm \textbf{0.06}$	-0.20 ± 0.07

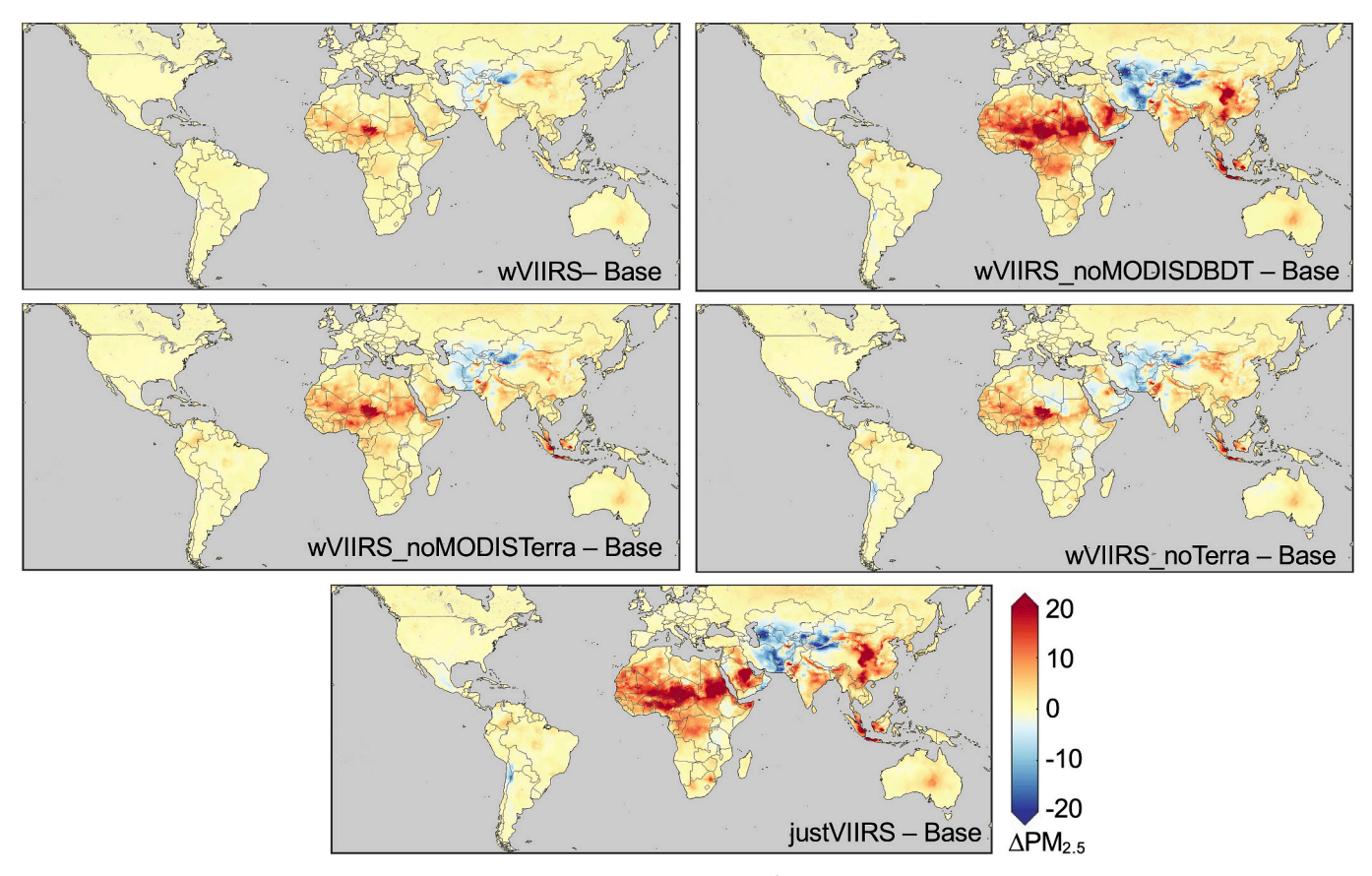


Fig. 7. The difference between the 2012 to 2019 mean hybrid $PM_{2.5}$ concentrations ($\mu g/m^3$) for each scenario from Table 1 and the Base scenario. Grey indicates missing data or water.

Data availability

Data will be made available on request.

Appendix A. Appendix

Table A1 The geophysical-hybrid $PM_{2.5}$ scenarios when including MAIAC.

Scenario	Description
Base _m	V4.GL.03 algorithm: includes MODIS Deep Blue and Dark Target from Terra (2000 to 2019) and Aqua (2002 to 2019), MODIS MAIAC (2000 to 2019), MISR (2000 to 2019), Sea WiFS (1997 to 2010) and GEOS-Chem simulated AOD (1998 to 2019).
wVIIRS _m	Base scenario with the addition of VIIRS Deep Blue and Dark Target for the VIIRS record (2012 to 2019)
$wVIIRS_{m}$ noMODISDBDT	wVIIRS scenario with the MODIS Deep Blue and Dark Target products from both Terra and Aqua removed
wVIIRS_noMODISTerra	wVIIRS scenario with all MODIS product from Terra removed (MODIS Deep, Dark Target, and MAIAC)
wVIIRS_noTerra	wVIIRS scenario with all Terra products removed (MODIS Deep Blue, Dark Target, MAIAC, and MISR)
justVIIRS	Scenario including just VIIRS Deep Blue, Dark Target, and GEOS-Chem simulated AOD

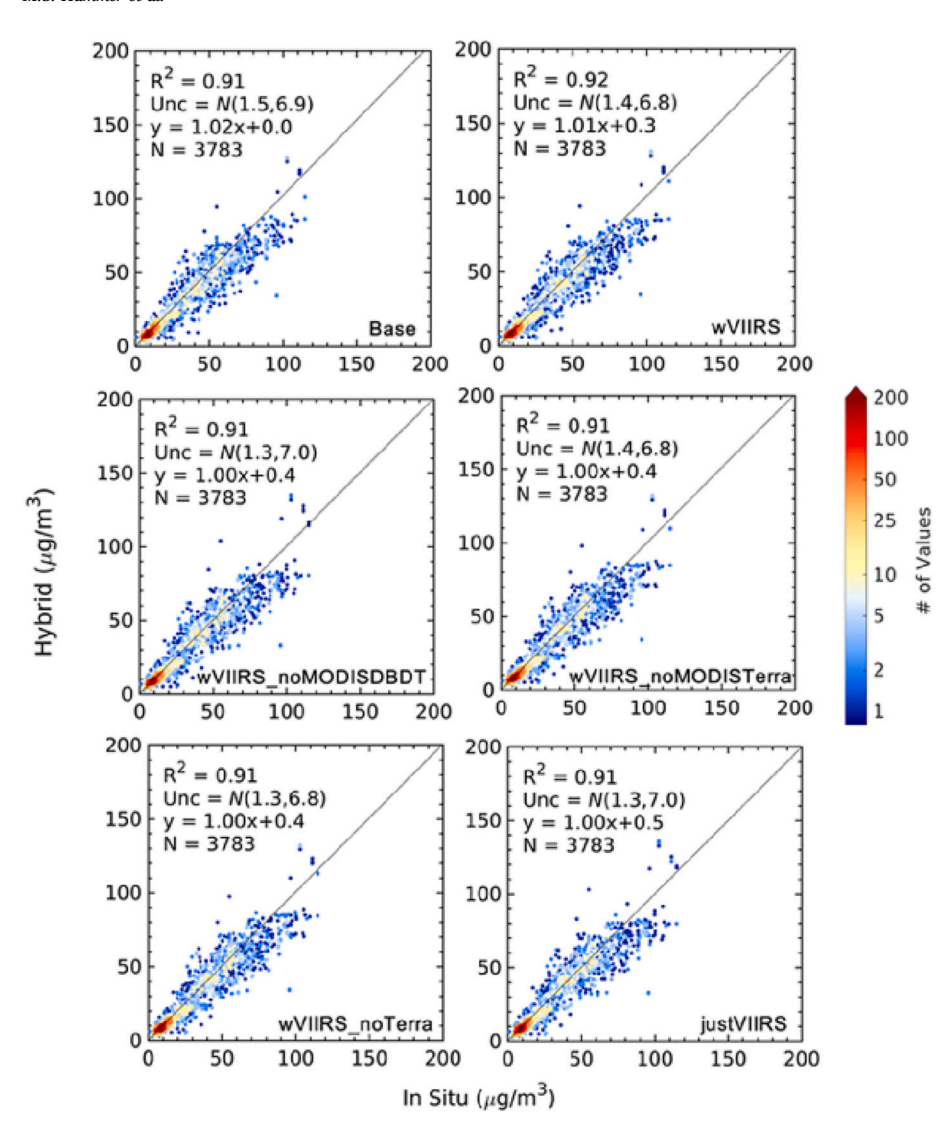


Fig. 8. Annual mean hybrid PM $_{2.5}$ concentrations for each scenario from Table 1 for 2015 versus collocated annual mean in situ values for 2015. The comparison was conducted using 10-fold out-of-sample 10% cross validation at sites that were not used in the GWR regression. Included on the plots are the coefficient of determination (R^2), the normal distribution of uncertainty (N(bias, variance)), the line of best fit (y) using reduced major axis linear regression, and the number of comparison points (N). The color scale indicates the number density of observations at each point.

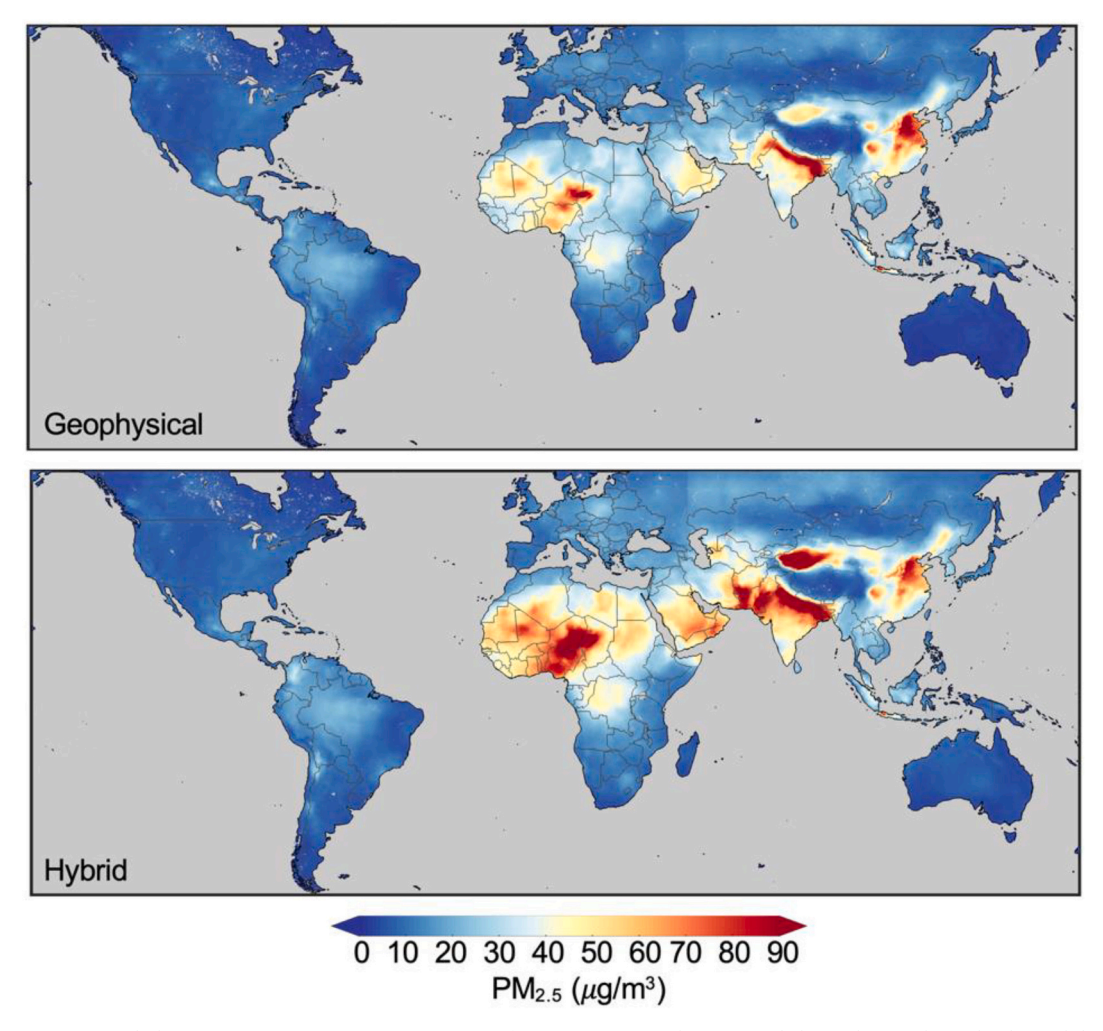


Fig. A1. The Base scenario (including MAIAC) mean $PM_{2.5}$ concentrations for 2012 to 2019. The top panel shows the geophysical values while the bottom panel shows the hybrid values. Grey indicates missing data or water.

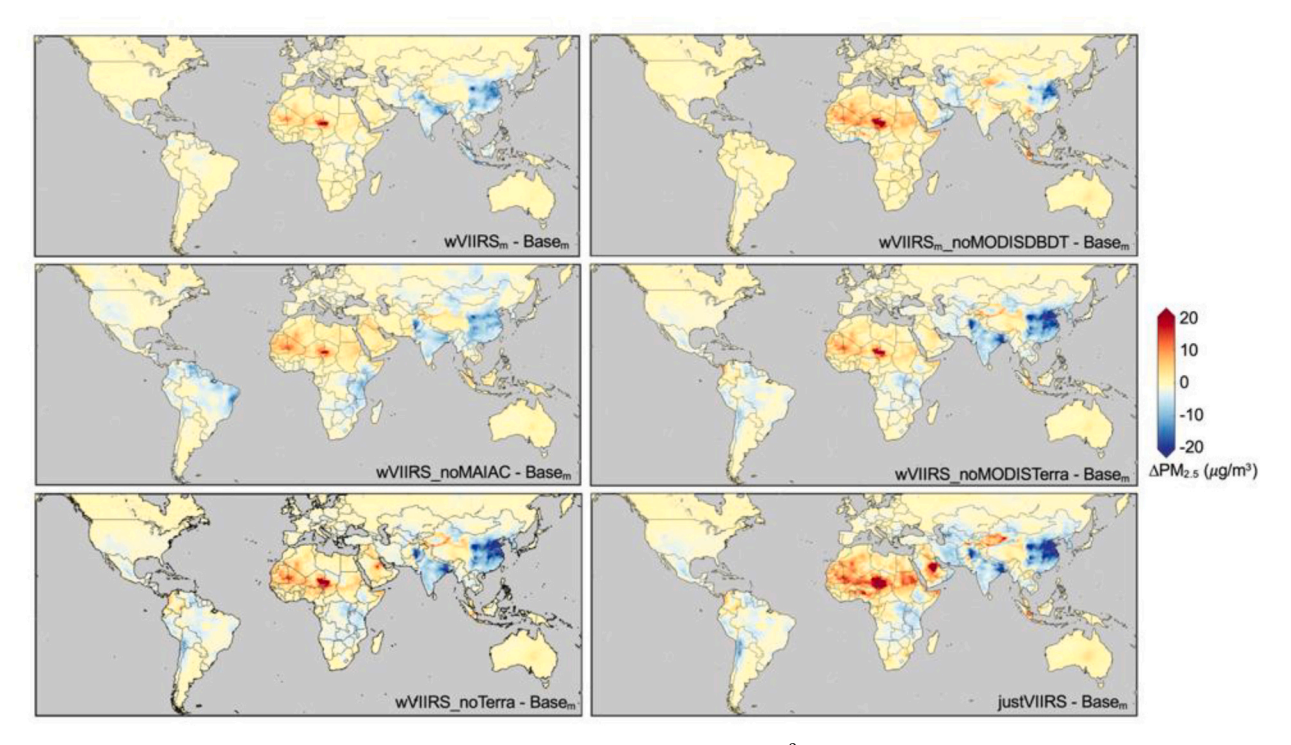


Fig. A2. The difference between the 2012 to 2019 mean geophysical $PM_{2.5}$ concentrations ($\mu g/m^3$) for each scenario from Table S2 and the Base scenario. Grey indicates missing data or water.

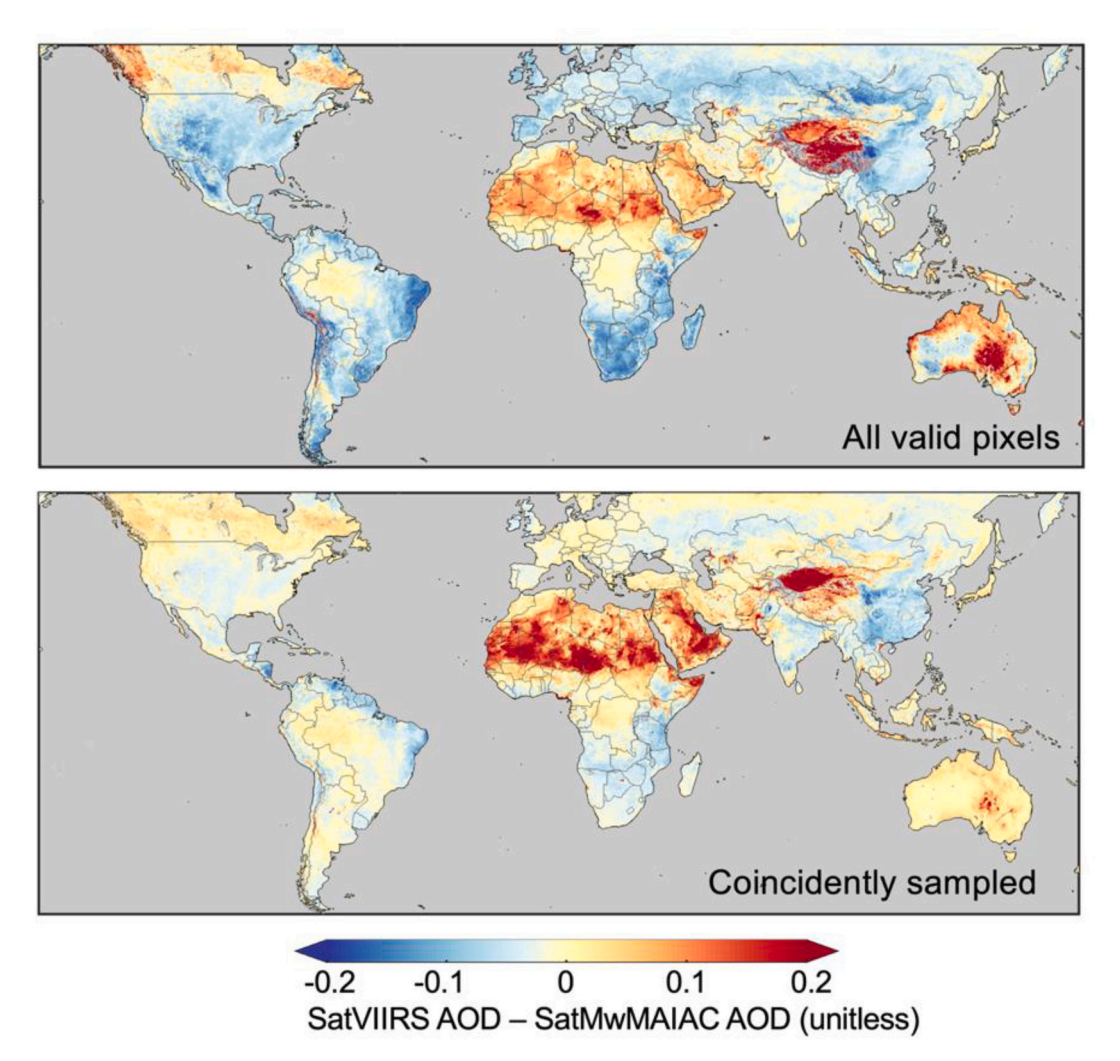


Fig. A3. Difference between the mean SatVIIRS AOD and the mean SatMwMAIAC AOD for 2012 to 2019. The SatVIIRS AOD includes VIIRS S-NPP Dark Target and Deep Blue, while SatMwMAIAC AOD includes MODIS Deep Blue and Dark Target from both Terra and Aqua, MISR, and MODIS MAIAC. For the top plot the means were calculated for all valid pixels and for the bottom plot the means only include coincidently sampled pixels between all products. Grey indicates missing data or water. (For interpretation of the references to color in this figure legend, the reader is referred to the web version of this article.)

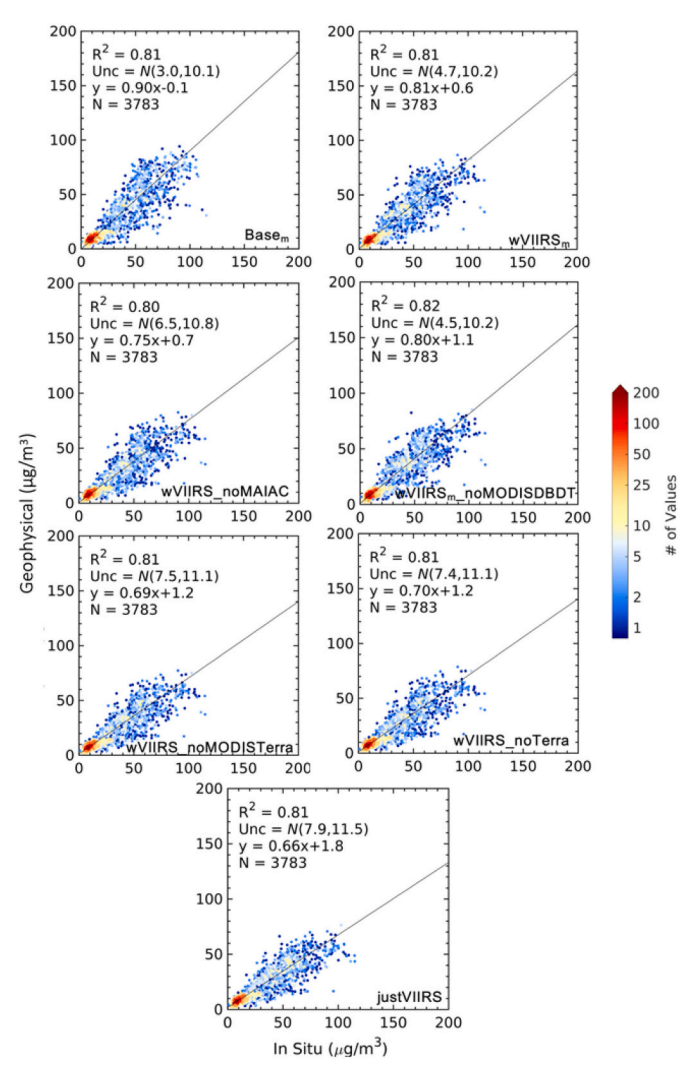


Fig. A4. Annual mean geophysical $PM_{2.5}$ concentrations for each scenario from Table S2 for 2015 versus collocated annual mean in situ values for 2015. Included on the plots are the coefficient of determination (R^2), the normal distribution of uncertainty (N(bias, variance)), the line of best fit (y) using reduced major axis linear regression, and the number of comparison points (N). The color scale indicates the number density of observations at each point.

Appendix A. Supplementary data

Supplementary data to this article can be found online at https://doi.org/10.1016/j.rse.2023.113624.

References

Anenberg, S.C., Henze, D.K., Tinney, V., Kinney, P.L., Raich, W., Fann, N., Malley, C.S., Roman, H., Lamsal, L., Duncan, B., Martin, R.V., van Donkelaar, A., Brauer, M., Doherty, R., Jonson, J.E., Davila, Y., Sudo, K., Kuylenstierna, J.C.I., 2018. Estimates of the global burden of ambient PM_{2.5}, ozone, and NO₂ on asthma incidence and emergency room visits. Environ. Health Perspect. 126 https://doi.org/10.1289/EHP3766.

Bai, L., Shin, S., Burnett, R.T., Kwong, J.C., Hystad, P., van Donkelaar, A., Goldberg, M. S., Lavigne, E., Copes, R., Martin, R.V., Kopp, A., Chen, H., 2019. Exposure to ambient air pollution and the incidence of congestive heart failure and acute myocardial infarction: a population-based study of 5.1 million Canadian adults living in Ontario. Environ. Int. 132, 105004 https://doi.org/10.1016/J. ENVINT.2019.105004.

Bey, I., Jacob, D.J., Yantosca, R.M., Logan, J.A., Field, B.D., Fiore, A.M., Li, Q., Liu, H.Y., Mickley, L.J., Schultz, M.G., 2001. Global modeling of tropospheric chemistry with assimilated meteorology: Model description and evaluation. J. Geophys. Res. 106, 23073. https://doi.org/10.1029/2001JD000807.

Brunsdon, C., Fotheringham, S., Charlton, M., 1998. Geographically weighted regression. J. Roy. Stat. Soc. Ser. D (The Statistician) 47, 431–443. https://doi.org/10.1111/1467-9884.00145.

Burnett, R., Chen, H., Szyszkowicz, M., Fann, N., Hubbell, B., Pope, C.A., Apte, J.S., Brauer, M., Cohen, A., Weichenthal, S., Coggins, J., Di, Q., Brunekreef, B.,

Frostad, J., Lim, S.S., Kan, H., Walker, K.D., Thurston, G.D., Hayes, R.B., Lim, C.C., Turner, M.C., Jerrett, M., Krewski, D., Gapstur, S.M., Diver, W.R., Ostro, B., Goldberg, D., Crouse, D.L., Martin, R.V., Peters, P., Pinault, L., Tjepkema, M., van Donkelaar, A., Villeneuve, P.J., Miller, A.B., Yin, P., Zhou, M., Wang, L., Janssen, N. A.H., Marra, M., Atkinson, R.W., Tsang, H., Thach, T.Q., Cannon, J.B., Allen, R.T., Hart, J.E., Laden, F., Cesaroni, G., Forastiere, F., Weinmayr, G., Jaensch, A., Nagel, G., Concin, H., Spadaro, J.V., 2018. Global estimates of mortality associated with longterm exposure to outdoor fine particulate matter. Proc. Natl. Acad. Sci. U. S. A. 115, 9592–9597. https://doi.org/10.1073/PNAS.1803222115.

CIESIN (Center for International Earth Science Information Network), 2017. Gridded Population of the World Version, p. 4. https://doi.org/10.1128/AAC.03728-14.

Diner, D.J., Beckert, J.C., Reilly, T.H., Bruegge, C.J., Conel, J.E., Kahn, R.A., Martonchik, J.V., Ackerman, T.P., Davies, R., Gerstl, S.A.W., Gordon, H.R., Muller, J., Myneni, R.B., Sellers, P.J., Pinty, B., Verstraete, M.M., 1998. Multi-angle Imaging SpectroRadiometer (MISR) instrument description and experiment overview. IEEE Trans. Geosci. Remote Sens. 36, 1072–1087. https://doi.org/ 10.1109/36.700992.

Fotheringham, A.S., Charlton, M.E., Brunsdon, C., 1998. Geographically weighted regression: a natural evolution of the expansion method for spatial data analysis. Environ. Plann. A Econ. Space 30, 1905–1927. https://doi.org/10.1068/a301905.

Garay, M.J., Kalashnikova, O.V., Bull, M.A., 2017. Development and assessment of a higher-spatial-resolution (4.4 km) MISR aerosol optical depth product using AERONET-DRAGON data. Atmos. Chem. Phys. 17, 5095–5106. https://doi.org/ 10.5194/acp-17-5095-2017.

- Garay, M.J., Witek, M.L., Kahn, R.A., Seidel, F.C., Limbacher, J.A., Bull, M.A., Diner, D. J., Hansen, E.G., Kalashnikova, O.V., Lee, H., Nastan, A.M., Yu, Y., 2020. Introducing the 4.4km spatial resolution Multi-Angle Imaging SpectroRadiometer (MISR) aerosol product. Atmos Meas. Tech. 13, 593–628. https://doi.org/10.5194/amt-13-593-2020.
- Gelaro, R., McCarty, W., Suárez, M.J., Todling, R., Molod, A., Takacs, L., Randles, C.A., Darmenov, A., Bosilovich, M.G., Reichle, R., Wargan, K., Coy, L., Cullather, R., Draper, C., Akella, S., Buchard, V., Conaty, A., da Silva, A.M., Gu, W., Kim, G.-K., Koster, R., Lucchesi, R., Merkova, D., Nielsen, J.E., Partyka, G., Pawson, S., Putman, W., Rienecker, M., Schubert, S.D., Sienkiewicz, M., Zhao, B., Gelaro, R., McCarty, W., Suárez, M.J., Todling, R., Molod, A., Takacs, L., Randles, C.A., Darmenov, A., Bosilovich, M.G., Reichle, R., Wargan, K., Coy, L., Cullather, R., Draper, C., Akella, S., Buchard, V., Conaty, A., da Silva, A.M., Gu, W., Kim, G.-K., Koster, R., Lucchesi, R., Merkova, D., Nielsen, J.E., Partyka, G., Pawson, S., Putman, W., Rienecker, M., Schubert, S.D., Sienkiewicz, M., Zhao, B., 2017. The Modern-Era Retrospective Analysis for Research and Applications, Version 2 (MERRA-2). J. Clim. 30, 5419–5454. https://doi.org/10.1175/JCLI-D-16-0758.1.
- Giles, D.M., Sinyuk, A., Sorokin, M.G., Schafer, J.S., Smirnov, A., Slutsker, I., Eck, T.F., Holben, B.N., Lewis, J.R., Campbell, J.R., Welton, E.J., Korkin, S.V., Lyapustin, A.I., 2019. Advancements in the Aerosol Robotic Network (AERONET) Version 3 database – automated near-real-time quality control algorithm with improved cloud screening for Sun photometer aerosol optical depth (AOD) measurements. Atmos Meas. Tech. 12, 169–209. https://doi.org/10.5194/amt-12-169-2019.
- Gupta, P., Levy, R.C., Mattoo, S., Remer, L.A., Munchak, L.A., 2016. A surface reflectance scheme for retrieving aerosol optical depth over urban surfaces in MODIS Dark Target retrieval algorithm. Atmos Meas. Tech. 9, 3293–3308. https://doi.org/ 10.5194/amt-9.3293-2016.
- Hammer, M.S., van Donkelaar, A., Li, C., Lyapustin, A., Sayer, A.M., Hsu, N.C., Levy, R. C., Garay, M.J., Kalashnikova, O.V., Kahn, R.A., Brauer, M., Apte, J.S., Henze, D.K., Zhang, L., Zhang, Q., Ford, B., Pierce, J.R., Martin, R.V., 2020. Global estimates and long-term trends of fine particulate matter concentrations (1998–2018). Environ. Sci. Technol. 54, 7879–7890. https://doi.org/10.1021/acs.est.0c01764.
- Hammer, M.S., van Donkelaar, A., Martin, R.V., McDuffie, E.E., Lyapustin, A., Sayer, A. M., Hsu, N.C., Levy, R.C., Garay, M.J., Kalashnikova, O.V., Kahn, R.A., 2021. Effects of COVID-19 lockdowns on fine particulate matter concentrations. Sci. Adv. 7, eabg7670. https://doi.org/10.1126/sciadv.abg7670.
- Hsu, N.C., Lee, J., Sayer, A.M., Kim, W., Bettenhausen, C., Tsay, S.-C., 2019. VIIRS Deep Blue aerosol products over land: extending the EOS long-term aerosol data records. J. Geophys. Res.-Atmos. 124, 4026–4053. https://doi.org/10.1029/2018JD029688.
- Kuhns, H., Knipping, E.M., Vukovich, J.M., 2005. Development of a United States-Mexico Emissions Inventory for the Big Bend Regional Aerosol and Visibility Observational (BRAVO) Study. J. Air Waste Manage. Assoc. 55, 677–692. https:// doi.org/10.1080/10473289.2005.10464648.
- Lee, J., Hsu, N.C., Sayer, A.M., Bettenhausen, C., Yang, P., 2017. AERONET-based nonspherical dust optical models and effects on the VIIRS Deep Blue/SOAR over water aerosol product. J. Geophys. Res.-Atmos. 122 https://doi.org/10.1002/ 2017JD027258, 10,384-10,401.
- Li, M., Zhang, Q., Kurokawa, J., Woo, J.-H., He, K., Lu, Z., Ohara, T., Song, Y., Streets, D. G., Carmichael, G.R., Cheng, Y., Hong, C., Huo, H., Jiang, X., Kang, S., Liu, F., Su, H., Zheng, B., 2017. MIX: a mosaic Asian anthropogenic emission inventory under the international collaboration framework of the MICS-Asia and HTAP. Atmos. Chem. Phys. 17, 935–963. https://doi.org/10.5194/acp-17-935-2017.
- Lu, Z., Zhang, Q., Streets, D.G., 2011. Sulfur dioxide and primary carbonaceous aerosol emissions in China and India. Atmos. Chem. Phys. Atmos. Chem. Phys. 11, 9839–9864. https://doi.org/10.5194/acp-11-9839-2011.
- Lyapustin, A., Wang, Y., Xiong, X., Meister, G., Platnick, S., Levy, R., Franz, B., Korkin, S., Hilker, T., Tucker, J., Hall, F., Sellers, P., Wu, A., Angal, A., 2014. Scientific impact of MODIS C5 calibration degradation and C6+ improvements. Atmos Meas. Tech. 7, 4353–4365. https://doi.org/10.5194/AMT-7-4353-2014.
- Lyapustin, A., Wang, Y., Korkin, S., Huang, D., 2018. MODIS collection 6 MAIAC algorithm. Atmos Meas. Tech. 11, 5741–5765. https://doi.org/10.5194/amt-11-5741-2018.
- Martin, R.V., Brauer, M., van Donkelaar, A., Shaddick, G., Narain, U., Dey, S., 2019. No one knows which city has the highest concentration of fine particulate matter. Atmos Environ X 3, 100040. https://doi.org/10.1016/J.AEAOA.2019.100040.
- Martins, V.S., Lyapustin, A., De Carvalho, L.A.S., Barbosa, C.C.F., Novo, E.M.L.M., 2017.
 Validation of high-resolution MAIAC aerosol product over South America.
 J. Geophys. Res.-Atmos. 122, 7537–7559. https://doi.org/10.1002/2016JD026301.
- Martonchik, J.V., Kahn, R.A., Diner, D.J., 2009. Retrieval of aerosol properties over land using MISR observations. In: Satellite Aerosol Remote Sensing over Land. Springer, Berlin Heidelberg, Berlin, Heidelberg, pp. 267–293. https://doi.org/10.1007/978-3-540-69397-0 9.
- Murray, C.J.L., Aravkin, A.Y., Zheng, P., Abbafati, C., Abbas, K.M., Abbasi Kangevari, M., Abd Allah, F., Abdelalim, A., Abdollahi, M., Abdollahpour, I., Abegaz, K.H., Abolhassani, H., Aboyans, V., Abreu, L.G., Abrigo, M.R.M., Abualhasan, A., Abu Raddad, L.J., Abushouk, A.I., Adabi, M., Adekambi, V., Adeoye, A.M., Adetokunboh, O.O., Adham, D., Advani, S.M., Agarwal, G., Aghamir, S.M.K., Agrawal, A., Ahmad, T., Ahmadi, K., Ahmadi, M., Ahmadieh, H., Ahmed, M.B., Akalu, T.Y., Akinyemi, R.O., Akinyemiju, T., Akombi, B., Akunna, C.J., Alahdab, F., Al Aly, Z., Alam, K., Alam, S., Alam, T., Alanezi, F.M., Alanzi, T.M., Alemu, B. Wassihun, Alhabib, K.F., Ali, M., Ali, S., Alicandro, G., Alinia, C., Alipour, V., Alizade, H., Aljunid, S.M., Alla, F., Allebeck, P., Almasi Hashiani, A., Al Mekhlafi, H.M., Alonso, J., Altirkawi, K.A., Amini Rarani, M., Amiri, F., Amugsi, D.A., Ancuceanu, R., Anderlini, D., Anderson, J.A., Andrei, C.L., Andrei, T., Angus, C., Anjomshoa, M., Ansari, F., Ansari Moghaddam, A., Antonazzo, I.C., Antonio, C.A.T., Antony, C.M., Antriyandarti, E., Anvari, D., Anwer, R., Appiah, S.C.

Y., Arabloo, J., Arab - Zozani, M., Ariani, F., Armoon, B., Ärnlöv, J., Arzani, A., Asadi - Aliabadi, M., Asadi - Pooya, A.A., Ashbaugh, C., Assmus, M., Atafar, Z., Atnafu, D. D., Atout, M.M.W., Ausloos, F., Ausloos, M., Ayala Quintanilla, B.P., Ayano, G. Ayanore, M.A., Azari, S., Azarian, G., Azene, Z.N., Badawi, A., Badiye, A.D., Bahrami, M.A., Bakhshaei, M.H., Bakhtiari, A., Bakkannavar, S.M., Baldasseroni, A., Ball, K., Ballew, S.H., Balzi, D., Banach, M., Banerjee, S.K., Bante, A.B., Baraki, A.G., Barker - Collo, S.L., Bärnighausen, T.W., Barrero, L.H., Barthelemy, C.M., Barua, L., Basu, S., Baune, B.T., Bayati, M., Becker, J.S., Bedi, N., Beghi, E., Béjot, Y., Bell, M.L., Bennitt, F.B., Bensenor, I.M., Berhe, K., Berman, A.E., Bhagavathula, A.S., Bhageerathy, R., Bhala, N., Bhandari, D., Bhattacharyya, K., Bhutta, Z.A., Bijani, A., Bikbov, B., Bin Sayeed, M.S., Biondi, A., Birihane, B.M., Bisignano, C., Biswas, R.K., Bitew, H., Bohlouli, S., Bohluli, M., Boon - Dooley, A.S., Borges, G., Borzì, A.M., Borzouei, S., Bosetti, C., Boufous, S., Braithwaite, D., Breitborde, N.J.K., Breitner, S., Brenner, H., Briant, P.S., Briko, A.N., Briko, N.I., Britton, G.B., Bryazka, D., Bumgarner, B.R., Burkart, K., Burnett, R.T., Burugina Nagaraja, S., Butt, Z.A., Caetano dos Santos, F.L., Cahill, L.E., Cámera, L.L.A., Campos - Nonato, I.R., Cárdenas, R., Carreras, G., Carrero, J.J., Carvalho, F., Castaldelli - Maia, J.M., Castañeda - Orjuela, C.A., Castelpietra, G., Castro, F., Causey, K., Cederroth, C.R., Cercy, K.M., Cerin, E., Chandan, J.S., Chang, K.-L., Charlson, F.J., Chattu, V.K., Chaturvedi, S., Cherbuin, N., Chimed - Ochir, O., Cho, D.Y., Choi, J.-Y.J., Christensen, H., Chu, D.-T., Chung, M.T., Chung, S.-C., Cicuttini, F.M., Ciobanu, L.G., Cirillo, M., Classen, T.K.D., Cohen, A.J., Compton, K., Cooper, O.R., Costa, V.M., Cousin, E., Cowden, R.G., Cross, D.H., Cruz, J.A., Dahlawi, S.M.A., Damasceno, A.A. M., Damiani, G., Dandona, L., Dandona, R., Dangel, W.J., Danielsson, A.-K., Dargan, P.I., Darwesh, A.M., Daryani, A., Das, J.K., das Gupta, Rajat, das Neves, J., Dávila - Cervantes, C.A., Davitoiu, D.V., de Leo, D., Degenhardt, L., DeLang, M., Dellavalle, R.P., Demeke, F.M., Demoz, G.T., Demsie, D.G., Denova - Gutiérrez, E., Dervenis, N., Dhungana, G.P., Dianatinasab, M., Dias da Silva, D., Diaz, D., Dibaji Forooshani, Z.S., Djalalinia, S., Do, H.T., Dokova, K., Dorostkar, F., Doshmangir, L., Driscoll, T.R., Duncan, B.B., Duraes, A.R., Eagan, A.W., Edvardsson, D., el Nahas, N., el Sayed, I., el Tantawi, M., Elbarazi, I., Elgendy, I.Y., El - Jaafary, S.I., Elyazar, I.R., Emmons - Bell, S., Erskine, H.E., Eskandarieh, S., Esmaeilnejad, S., Esteghamati, A., Estep, K., Etemadi, A., Etisso, A.E., Fanzo, J., Farahmand, M., Fareed, M., Faridnia, R., Farioli, A., Faro, A., Faruque, M., Farzadfar, F., Fattahi, N., Fazlzadeh, M., Feigin, V.L., Feldman, R., Fereshtehnejad, S.-M., Fernandes, E., Ferrara, G., Ferrari, A.J., Ferreira, M.L., Filip, I., Fischer, F., Fisher, J.L., Flor, L.S., Foigt, N.A., Folayan, M.O., Fomenkov, A.A., Force, L.M., Foroutan, M., Franklin, R. C., Freitas, M., Fu, W., Fukumoto, T., Furtado, J.M., Gad, M.M., Gakidou, E., Gallus, S., Garcia - Basteiro, A.L., Gardner, W.M., Geberemariyam, B.S., Gebreslassie, A.A.A.A., Geremew, A., Gershberg Hayoon, A., Gething, P.W., Ghadimi, M., Ghadiri, K., Ghaffarifar, F., Ghafourifard, M., Ghamari, F., Ghashghaee, A., Ghiasvand, H., Ghith, N., Gholamian, A., Ghosh, R., Gill, P.S., Ginindza, T.G.G., Giussani, G., Gnedovskaya, E.V., Goharinezhad, S., Gopalani, S.V., Gorini, G., Goudarzi, H., Goulart, A.C., Greaves, F., Grivna, M., Grosso, G., Gubari, M.I.M., Gugnani, H.C., Guimarães, R.A., Guled, R.A., Guo, G., Guo, Y., Gupta, Rajeev, Gupta, T., Haddock, B., Hafezi - Nejad, N., Hafiz, A., Haj Mirzaian, Arvin, Haj - Mirzaian, Arya, Hall, B.J., Halvaei, I., Hamadeh, R.R. Hamidi, S., Hammer, M.S., Hankey, G.J., Haririan, H., Haro, J.M., Hasaballah, A.I., Hasan, M.M., Hasanpoor, E., Hashi, A., Hassanipour, S., Hassankhani, H., Havmoeller, R.J., Hay, S.I., Hayat, K., Heidari, G., Heidari - Soureshjani, R., Henrikson, H.J., Herbert, M.E., Herteliu, C., Heydarpour, F., Hird, T.R., Hoek, H.W., Holla, R., Hoogar, P., Hosgood, H.D., Hossain, N., Hosseini, M., Hosseinzadeh, M., Hostiuc, M., Hostiuc, S., Househ, M., Hsairi, M., Hsieh, V.C., Hu, G., Hu, K., Huda, T. M., Humayun, A., Huynh, C.K., Hwang, B.-F., Iannucci, V.C., Ibitoye, S.E., Ikeda, N., Ikuta, K.S., Ilesanmi, O.S., Ilic, I.M., Ilic, M.D., Inbaraj, L.R., Ippolito, H., Iqbal, U., Irvani, S.S.N., Irvine, C.M.S., Islam, M.M., Islam, S.M.S., Iso, H., Ivers, R.Q., Iwu, C.C. D., Iwu, C.J., Iyamu, I.O., Jaafari, J., Jacobsen, K.H., Jafari, H., Jafarinia, M., Jahani, M.A., Jakovljevic, M., Jalilian, F., James, S.L., Janjani, H., Javaheri, T., Javidnia, J., Jeemon, P., Jenabi, E., Jha, R.P., Jha, V., Ji, J.S., Johansson, L., John, O., John - Akinola, Y.O., Johnson, C.O., Jonas, J.B., Joukar, F., Jozwiak, J.J., Jürisson, M., Kabir, A., Kabir, Z., Kalani, H., Kalani, R., Kalankesh, L.R., Kalhor, R., Kanchan, T., Kapoor, N., Karami Matin, B., Karch, A., Karim, M.A., Kassa, G.M., Katikireddi, S.V., Kayode, G.A., Kazemi Karyani, A., Keiyoro, P.N., Keller, C., Kemmer, L., Kendrick, P.J., Khalid, N., Khammarnia, M., Khan, E.A., Khan, M., Khatab, K., Khater, M.M., Khatib, M.N., Khayamzadeh, M., Khazaei, S., Kieling, C., Kim, Y.J., Kimokoti, R.W., Kisa, A., Kisa, S., Kivimäki, M., Knibbs, L.D., Knudsen, A. K.S., Kocarnik, J.M., Kochhar, S., Kopec, J.A., Korshunov, V.A., Koul, P.A., Koyanagi, A., Kraemer, M.U.G., Krishan, K., Krohn, K.J., Kromhout, H., Kuate Defo, B., Kumar, G.A., Kumar, V., Kurmi, O.P., Kusuma, D., la Vecchia, C., Lacey, B., Lal, D.K., Lalloo, R., Lallukka, T., Lami, F.H., Landires, I., Lang, J.J., Langan, S.M., Larsson, A.O., Lasrado, S., Lauriola, P., Lazarus, J.V., Lee, P.H., Lee, S.W.H., Le Grand, K.E., Leigh, J., Leonardi, M., Lescinsky, H., Leung, J., Levi, M., Li, S., Lim, L.-L., Linn, S., Liu, Shiwei, Liu, Simin, Liu, Y., Lo, J., Lopez, A.D., Lopez, J.C.F., Lopukhov, P.D., Lorkowski, S., Lotufo, P.A., Lu, A., Lugo, A., Maddison, E.R. Mahasha, P.W., Mahdavi, M.M., Mahmoudi, M., Majeed, A., Maleki, A., Maleki, S., Malekzadeh, R., Malta, D.C., Mamun, A.A., Manda, A.L., Manguerra, H., Mansour -Ghanaei, F., Mansouri, B., Mansournia, M.A., Mantilla Herrera, A.M., Maravilla, J.C., Marks, A., Martin, R.V., Martini, S., Martins - Melo, F.R., Masaka, A., Masoumi, S.Z., Mathur, M.R., Matsushita, K., Maulik, P.K., McAlinden, C., McGrath, J.J., McKee, M., Mehndiratta, M.M., Mehri, F., Mehta, K.M., Memish, Z.A., Mendoza, W., Menezes, R. G., Mengesha, E.W., Mereke, A., Mereta, S.T., Meretoja, A., Meretoja, T.J., Mestrovic, T., Miazgowski, B., Miazgowski, T., Michalek, I.M., Miller, T.R., Mills, E. J., Mini, G., Miri, M., Mirica, A., Mirrakhimov, E.M., Mirzaei, H., Mirzaei, M., Mirzaei, R., Mirzaei - Alavijeh, M., Misganaw, A.T., Mithra, P., Moazen, B., Mohammad, D.K., Mohammad, Y., Mohammad Gholi Mezerji, N., Mohammadian -Hafshejani, A., Mohammadifard, N., Mohammadpourhodki, R., Mohammed, A.S.,

Mohammed, H., Mohammed, J.A., Mohammed, S., Mokdad, A.H., Molokhia, M., Monasta, L., Mooney, M.D., Moradi, G., Moradi, M., Moradi - Lakeh, M., Moradzadeh, R., Moraga, P., Morawska, L., Morgado - da - Costa, J., Morrison, S.D., Mosapour, A., Mosser, J.F., Mouodi, S., Mousavi, S.M., Mousavi Khaneghah, A., Mueller, U.O., Mukhopadhyay, S., Mullany, E.C., Musa, K.I., Muthupandian, S. Nabhan, A.F., Naderi, M., Nagarajan, A.J., Nagel, G., Naghavi, M., Naghshtabrizi, B., Naimzada, M.D., Najafi, F., Nangia, V., Nansseu, J.R., Naserbakht, M., Nayak, V.C., Negoi, I., Ngunjiri, J.W., Nguyen, C.T., Nguyen, H.L.T., Nguyen, M., Nigatu, Y.T., Nikbakhsh, R., Nixon, M.R., Nnaji, C.A., Nomura, S., Norrving, B., Noubiap, J.J., Nowak, C., Nunez - Samudio, V., Oţoiu, A., Oancea, B., Odell, C.M., Ogbo, F.A., Oh, I.-H., Okunga, E.W., Oladnabi, M., Olagunju, A.T., Olusanya, B.O., Olusanya, J. O., Omer, M.O., Ong, K.L., Onwujekwe, O.E., Orpana, H.M., Ortiz, A., Osarenotor, O., Osei, F.B., Ostroff, S.M., Otstavnov, N., Otstavnov, S.S., Øverland, S., Owolabi, M.O.P.A.M., Padubidri, J.R., Palladino, R., Panda-Jonas, S., Pandey, A., Parry, C.D.H., Pasovic, M., Pasupula, D.K., Patel, S.K., Pathak, M., Patten, S.B., Patton, G.C., Pazoki Toroudi, H., Peden, A.E., Pennini, A., Pepito, V.C.F., Peprah, E. K., Pereira, D.M., Pesudovs, K., Pham, H.Q., Phillips, M.R., Piccinelli, C., Pilz, T.M., Piradov, M.A., Pirsaheb, M., Plass, D., Polinder, S., Polkinghorne, K.R., Pond, C.D., Postma, M.J., Pourjafar, H., Pourmalek, F., Poznańska, A., Prada, S.I., Prakash, V., Pribadi, D.R.A., Pupillo, E., Quazi Syed, Z., Rabiee, M., Rabiee, N., Radfar, A., Rafiee, A., Raggi, A., Rahman, M.A., Rajabpour-Sanati, A., Rajati, F., Rakovac, I., Ram, P., Ramezanzadeh, K., Ranabhat, C.L., Rao, P.C., Rao, S.J., Rashedi, V., Rathi, P., Rawaf, D.L., Rawaf, S., Rawal, L., Rawassizadeh, R., Rawat, R., Razo, C., Redford, S.B., Reiner, R.C., Reitsma, M.B., Remuzzi, G., Renjith, V., Renzaho, A.M. N., Resnikoff, S., Rezaei, Negar, Rezaei, Nima, Rezapour, A., Rhinehart, P.-A., Riahi, S.M., Ribeiro, D.C., Ribeiro, D., Rickard, J., Rivera, J.A., Roberts, N.L.S. Rodríguez-Ramírez, S., Roever, L., Ronfani, L., Room, R., Roshandel, G., Roth, G.A., Rothenbacher, D., Rubagotti, E., Rwegerera, G.M., Sabour, S., Sachdev, P.S., Saddik, B., Sadeghi, E., Sadeghi, M., Saeedi, R., Saeedi Moghaddam, S., Safari, Y., Safi, S., Safiri, S., Sagar, R., Sahebkar, A., Sajadi, S.M., Salam, N., Salamati, P., Salem, H., Salem, M.R.R., Salimzadeh, H., Salman, O.M., Salomon, J.A., Samad, Z., Samadi Kafil, H., Sambala, E.Z., Samy, A.M., Sanabria, J., Sánchez-Pimienta, T.G., Santomauro, D.F., Santos, I.S., Santos, J.V., Santric-Milicevic, M.M., Saraswathy, S.Y. I., Sarmiento-Suárez, R., Sarrafzadegan, N., Sartorius, B., Sarveazad, A., Sathian, B., Sathish, T., Sattin, D., Saxena, S., Schaeffer, L.E., Schiavolin, S., Schlaich, M.P., Schmidt, M.I., Schutte, A.E., Schwebel, D.C., Schwendicke, F., Senbeta, A.M., Senthilkumaran, S., Sepanlou, S.G., Serdar, B., Serre, M.L., Shadid, J., Shafaat, O., Shahabi, S., Shaheen, A.A., Shaikh, M.A., Shalash, A.S., Shams-Beyranvand, M. Shamsizadeh, M., Sharafi, K., Sheikh, A., Sheikhtaheri, A., Shibuya, K., Shield, K.D., Shigematsu, M., Shin, J. Il, Shin, M.-J., Shiri, R., Shirkoohi, R., Shuval, K., Siabani, S., Sierpinski, R., Sigfusdottir, I.D., Sigurvinsdottir, R., Silva, J.P., Simpson, K.E., Singh, J.A., Singh, P., Skiadaresi, E., Skou, S.T.S., Skryabin, V.Y., Smith, E.U.R., Soheili, A., Soltani, S., Soofi, M., Sorensen, R.J.D., Soriano, J.B., Sorrie, M.B., Soshnikov, S., Soyiri, I.N., Spencer, C.N., Spotin, A., Sreeramareddy, C. T., Srinivasan, V., Stanaway, J.D., Stein, C., Stein, D.J., Steiner, C., Stockfelt, L., Stokes, M.A., Straif, K., Stubbs, J.L., Sufiyan, M.B., Suleria, H.A.R., Suliankatchi Abdulkader, R., Sulo, G., Sultan, I., Szumowski, Ł., Tabarés-Seisdedos, R., Tabb, K. M., Tabuchi, T., Taherkhani, A., Tajdini, M., Takahashi, K., Takala, J.S., Tamiru, A. T., Taveira, N., Tehrani-Banihashemi, A., Temsah, M.-H., Tesema, G.A., Tessema, Z. T., Thurston, G.D., Titova, M.V., Tohidinik, H.R., Tonelli, M., Topor-Madry, R., Topouzis, F., Torre, A.E., Touvier, M., Tovani-Palone, M.R.R., Tran, B.X., Travillian, R., Tsatsakis, A., Tudor Car, L., Tyrovolas, S., Uddin, R., Umeokonkwo, C. D., Unnikrishnan, B., Upadhyay, E., Vacante, M., Valdez, P.R., van Donkelaar, A., Vasankari, T.J., Vasseghian, Y., Veisani, Y., Venketasubramanian, N., Violante, F.S., Vlassov, V., Vollset, S.E., Vos, T., Vukovic, R., Waheed, Y., Wallin, M.T., Wang, Y., Wang, Y.-P., Watson, A., Wei, J., Wei, M.Y.W., Weintraub, R.G., Weiss, J., Werdecker, A., West, J.J., Westerman, R., Whisnant, J.L., Whiteford, H.A., Wiens, K. E., Wolfe, C.D.A., Wozniak, S.S., Wu, A.-M., Wu, J., Wulf Hanson, S., Xu, G., Xu, R., Yadgir, S., Yahyazadeh Jabbari, S.H., Yamagishi, K., Yaminfirooz, M., Yano, Y., Yaya, S., Yazdi-Feyzabadi, V., Yeheyis, T.Y., Yilgwan, C.S., Yilma, M.T., Yip, P., Yonemoto, N., Younis, M.Z., Younker, T.P., Yousefi, B., Yousefi, Z., Yousefinezhadi, T., Yousuf, A.Y., Yu, C., Yusefzadeh, H., Zahirian Moghadam, T., Zamani, M., Zamanian, M., Zandian, H., Zastrozhin, M.S., Zhang, Y., Zhang, Z.-J.,

- Zhao, J.T., Zhao, X.-J.G., Zhao, Y., Zhou, M., Ziapour, A., Zimsen, S.R.M., Brauer, M., Afshin, A., Lim, S.S., 2020. Global burden of 87 risk factors in 204 countries and territories, 1990–2019: a systematic analysis for the Global Burden of Disease Study 2019. Lancet 396, 1223–1249. https://doi.org/10.1016/S0140-6736(20)30752-2.
- Odo, D.B., Yang, I.A., Dey, S., Hammer, M.S., van Donkelaar, A., Martin, R.V., Dong, G. H., Yang, B.Y., Hystad, P., Knibbs, L.D., 2022. Ambient air pollution and acute respiratory infection in children aged under 5 years living in 35 developing countries. Environ. Int. 159, 107019 https://doi.org/10.1016/J. ENVINT 2021 107019
- Pappin, A.J., Christidis, T., Pinault, L.L., Crouse, D.L., Brook, J.R., Erickson, A., Hystad, P., Li, C., Martin, R.V., Meng, J., Weichenthal, S., van Donkelaar, A., Tjepkema, M., Brauer, M., Burnett, R.T., 2019. Examining the shape of the association between low levels of fine particulate matter and mortality across three cycles of the Canadian Census Health and Environment Cohort. Environ. Health Perspect. 127 https://doi.org/10.1289/EHP5204.
- Sawyer, V., Levy, R.C., Mattoo, S., Cureton, G., Shi, Y., Remer, L.A., 2020. Continuing the MODIS dark target aerosol time series with VIIRS. Remote Sens. 12, 308. https://doi. org/10.3390/RS12020308.
- Sayer, A.M., Hsu, N.C., Bettenhausen, C., Jeong, M.-J., Holben, B.N., Zhang, J., 2012. Global and regional evaluation of over-land spectral aerosol optical depth retrievals from SeaWiFS. Atmos Meas. Tech. 5, 1761–1778. https://doi.org/10.5194/amt-5-1761-2012
- Sayer, A.M., Hsu, N.C., Lee, J., Kim, W.V., Dutcher, S.T., 2019. Validation, stability, and consistency of MODIS collection 6.1 and VIIRS version 1 Deep Blue aerosol data over land. J. Geophys. Res.-Atmos. 124, 4658–4688. https://doi.org/10.1029/2018JD029598.
- Southerland, V.A., Brauer, M., Mohegh, A., Hammer, M.S., van Donkelaar, A., Martin, R. V., Apte, J.S., Anenberg, S.C., 2022. Global urban temporal trends in fine particulate matter (PM_{2.5}) and attributable health burdens: estimates from global datasets. Lancet Planet Health 0. https://doi.org/10.1016/S2542-5196(21)00350-8.
- Travis, K.R., Jacob, D.J., Fisher, J.A., Kim, P.S., Marais, E.A., Zhu, L., Yu, K., Miller, C.C., Yantosca, R.M., Sulprizio, M.P., Thompson, A.M., Wennberg, P.O., Crounse, J.D., St. Clair, J.M., Cohen, R.C., Laughner, J.L., Dibb, J.E., Hall, S.R., Ullmann, K., Wolfe, G. M., Pollack, I.B., Peischl, J., Neuman, J.A., Zhou, X., 2016. Why do models overestimate surface ozone in the Southeast United States? Atmos. Chem. Phys. 16, 13561–13577. https://doi.org/10.5194/acp-16-13561-2016.
- van Donkelaar, A., Martin, R.V., Park, R.J., 2006. Estimating ground-level PM_{2.5} using aerosol optical depth determined from satellite remote sensing. J. Geophys. Res. 111, 21201. https://doi.org/10.1029/2005JD006996.
- van Donkelaar, A., Martin, R.V., Brauer, M., Hsu, N.C., Kahn, R.A., Levy, R.C., Lyapustin, A., Sayer, A.M., Winker, D.M., 2016. Global estimates of fine particulate matter using a combined geophysical-statistical method with information from satellites, models, and monitors. Environ. Sci. Technol. 50, 3762–3772. https://doi. org/10.1021/acs.est.5b05833.
- van Donkelaar, A., Martin, R.V., Li, C., Burnett, R.T., 2019. Regional estimates of chemical composition of fine particulate matter using a combined geosciencestatistical method with information from satellites, models, and monitors. Environ. Sci. Technol. 53, 2595–2611. https://doi.org/10.1021/acs.est.8b06392.
- van Donkelaar, A., Hammer, M.S., Bindle, L., Brauer, M., Brook, J.R., Garay, M.J., Hsu, N.C., Kalashnikova, O.V., Kahn, R.A., Lee, C., Levy, R.C., Lyapustin, A., Sayer, A.M., Martin, R.V., 2021. Monthly global estimates of fine particulate matter and their uncertainty. Environ. Sci. Technol. acs.est.1c05309 https://doi.org/10.1021/ACS.EST.1C05309.
- Wolfe, R.E., Lin, G., Nishihama, M., Tewari, K.P., Tilton, J.C., Isaacman, A.R., 2013. Suomi NPP VIIRS prelaunch and on-orbit geometric calibration and characterization. J. Geophys. Res.-Atmos. 118 https://doi.org/10.1002/JGRD.50873, 11,508-11,521.
- World Health Organization, 2018. WHO Global Ambient Air Quality Database (update 2018)
- Xiong, X., Angal, A., Chang, T., Chiang, K., Lei, N., Li, Y., Sun, J., Twedt, K., Wu, A., 2020. MODIS and VIIRS calibration and characterization in support of producing long-term high-quality data Products. Remote Sens. 12, 3167. https://doi.org/10.3390/RS12193167. 2020.